VYSOKÉ UČENÍ TECHNICKÉ V BRNĚ
BRNO UNIVERSITY OF TECHNOLOGY

FAKULTA STROJNÍHO INŽENÝRSTVÝ
ÚSTAV FYZIKÁLNÍHO INŽENÝRSTVÝ

FACULTY OF MECHANICAL ENGINEERING
INSTITUTE OF PHYSICAL ENGINEERING

PLASMON-ENHANCED PHOTOLUMINESCENCE

FOTOLUMINISCENCE ZESÍLENÁ PLAZMONOVÝMI POLARITONY

DIPLOMOVÁ PRÁCE
MASTER`S THESIS

AUTOR PRÁCE — Bc. ZOLTÁN ÉDES
AUTHOR

VEDOUCÍ PRÁCE — Prof. RNDr. TOMÁŠ ŠIKOLA, CSs.
SUPERVISOR

BRNO 2012

Vysoké učení technické v Brně, Fakulta strojního inženýrství

Ústav fyzikálního inženýrství
Akademický rok: 2011/12

ZADÁNÍ DIPLOMOVÉ PRÁCE

student(ka): Bc. Zoltán Édes

který/která studuje v **magisterském studijním programu**

obor: **Fyzikální inženýrství a nanotechnologie (3901T043)**

Ředitel ústavu Vám v souladu se zákonem č.111/1998 o vysokých školách a se Studijním a zkušebním řádem VUT v Brně určuje následující téma diplomové práce:

Fotoluminiscence zesílená plazmonovými polaritony

v anglickém jazyce:

Plasmon enhanced photoluminescence

Stručná charakteristika problematiky úkolu:

1. Proveďte rešeršní studii fyzikálních základů interakce povrchových plazmonových polaritonů s fotoluminiscenčně aktivními látkami s ohledem na jejich využití v oblasti nanofotoniky.
2. Navrhněte a sestavte aparaturu pro měření fotoluminiscence planárních vzorků. Ověřte a specifikujte fotoluminiscenční vlastnosti vybraných vzorků (např. GaN, CdTe nanoteček a ncSi).
3.Navrhněte technologický postup přípravy vzorků sestávajících z kovových nanostruktur a fotoluminiscenčních objektů a metodu měření fotoluminiscence těchto objektů zesílené plazmonovými efekty.

Cíle diplomové práce:

Ověření možnosti zesílení fotoluminiscence pevných látek pomocí povrchových plazmonových polaritonů.

Seznam odborné literatury:

1. Stefan Maier, Plasmonics: Fundamentals and Applications, Springer Science Business Media LLC, 2007.

2. I. Pelant a J. Valenta: Luminiscenční spektroskopie II. díl, Academia Praha 2010.

Vedoucí diplomové práce: prof. RNDr. Tomáš Šikola, CSc.

Termín odevzdání diplomové práce je stanoven časovým plánem akademického roku 2011/12.

V Brně, dne 25.11.2011

L.S.

VYSOKÉ UČENÍ TECHNICKÉ V BRNĚ
FAKULTA STROJNÍHO INŽENÝRSTVÍ
DĚKANÁT

prof. RNDr. Tomáš Šikola, CSc.
Ředitel ústavu

prof. RNDr. Miroslav Doupovec, CSc.
Děkan

Abstrakt

Diplomová práce se zabývá fotoluminiscencí polovodičových materiálů zesílené plazmonovými polaritony. Je popsána základní teorie interakce mezi lokalizovanými povrchovými plazmony a fotoluminiscenčními látkami. Dva mechanismy, které mohou vést k fotoluminiscenci zesílené plazmonovými polaritony jsou diskutovány. Následně je popsán návrh aparatury pro měření fotoluminiscence a způsob její realizace. Funkčnost aparatury je ověřena měřením fotoluminiscenčních spekter objemového GaN, nanokrystalického Si a CdTe kvantových teček. Nakonec je zkoumána metoda přípravy vzorků sestávajících z kovových nanokuliček a fotoluminiscenčně aktívních CdTe kvantových teček.

Summary

The diploma thesis deals with plasmon-enhanced photoluminescence in semiconductors. Fistly, the basic theory of the interaction between localized surface plasmons and photoluminescent materials is described. Two mechanisms leading to plasmon-enhanced photoluminescence are discussed. Subsequently, the design of the apparatus for measuring photoluminescence is depicted and the way of its assembly described. Functionality of the apparatus is tested by measuring photoluminescence spectra of bulk GaN, nanocrystalline Si and CdTe quantum dots. Finally, the preparation method of samples consisting of metal nanospheres and photoluminescence active CdTe quantum dots is investigated.

Klíčová slova

plazmonika, lokalizované povrchové plazmony, fotoluminiscence, kvantové tečky

Keywords

plasmonics, localized surface plasmons, photoluminescene, quantum dots

ÉDES, Z. *Fotoluminiscence zesílená plazmonovými polaritony.* Brno: Vysoké učení technické v Brně, Fakulta strojního inženýrství, 2012. 65 s. Vedoucí diplomové práce prof. RNDr. Tomáš Šikola, CSc.

Prohlášení

Prohlašuji, že jsem tuto diplomovou práci vypracoval samostatně, pouze pod odborným vedením prof. RNDr. Tomáše Šikoly, CSc. a s použitím literatury, kterou uvádím v seznamu použité literatury.

V Brně 25. května 2012

Poděkování

Děkuji prof. RNDr. Tomáši Šikolovi, CSc za odborné vedení, konzultace a opravy při psaní této práce. Zároveň bych rád poděkoval Mgr. Tomáši Šamořilovi za pomoc při provedení experimentů, dále Ing. Lukáši Břínkovi a Ing. Miroslavu Kolíbalovi Ph.D. za konzultace a cenné rady během psaní této práce.
Soli Deo Gloria!

Contents

Introduction

Photoluminescence is a spontaneus light emission of materials following optical excitation. This phenomenon was observed in the nature from the ancient times. In China and Japan photoluminescent pigments were used as early as 1000 years ago. The first scientific study of photoluminescence started in the 17th century by discovering the “bolognian stone“ (BaS). The term “phosphorescence“ was introduced for a sustained emission after termination of excitation and “fluorescence“ for a fast decaying emission. The therm “photoluminescence“ was used first at the end of the 19th century and it includes phosphorescence and fluorescence as well. The rigorous description of photoluminescence came only in the 20th century thanks to the quantum physics. In the 20th century photoluminescence started to be used in various applications of microscopy and in research of organic materials, and also in spectroscopy. More recently, photoluminescent materials are used in ligth emitting devices as laser diodes and in biology and medicine for sensing and imaging.

Since in 1946 Edward Mills Purcell reported that emission properties of materials are influenced with the environment in which the emitter is placed [1], the possibilities to enhance luminescence have been widely investigated. It was already reported in the 70s and 80s of the last century that metal surfaces or small particles in the proximity of emitter can strongly enhance or quenche photoluminescence due to the excitation of surface plasmon polaritons. Surface plasmon polaritons are collective oscillations of electrons at metal interfaces coupled to the electromagnetic field.

The plasmon-enhanced luminescence was well described theoretically in the 80s, but the efforts for its application have intensified only since the past decade due to the appearance of advanced fabrication and characterisation methods at nanoscale.

This thesis deals with the theoretical description of plasmon-enhanced photoluminescence. Furthermore, the experimental part of the thesis contains the design and realization of an apparatus for measuring photoluminescence and the results of the measurements carried out using the apparatus. Finally, preparation methods of samples for studying the enhanced photoluminescene are shortly investigated.

1 Theoretical foundations

This chapter contains the brief introduction to the theory of electromagnetic field and to the optical properties of metals in order to understand existence and behaviour of surface plasmon polaritons.

1.1 Maxwell's equations

The fundamental equations describing electromagnetic field in vacuum and in different media are the Maxwell's equations.

$$\nabla . \boldsymbol{D} = \rho_{ext} \tag{1.1}$$

$$\nabla . \boldsymbol{B} = 0 \tag{1.2}$$

$$\nabla \times \boldsymbol{E} = -\frac{\partial \boldsymbol{B}}{\partial t} \tag{1.3}$$

$$\nabla \times \boldsymbol{H} = \boldsymbol{J} + \frac{\partial \boldsymbol{D}}{\partial t} \tag{1.4}$$

This is the differential form of the macroscopic Maxwell equations, which are describing every electromagnetic phenomenon and link the electric and magnetic field. Dielectric displacement $\boldsymbol{D}$ and intensity of electric field $\boldsymbol{E}$ are further inetrconnected with the equation

$$\boldsymbol{D} = \varepsilon_0 \boldsymbol{E} + \boldsymbol{P}, \tag{1.5}$$

where ε_0 is the permittivity of the vacuum and $\boldsymbol{P}$ is the polarization.

Magnetic induction $\boldsymbol{B}$ and magnetic intensity $\boldsymbol{H}$ are linked through the equation:

$$\boldsymbol{H} = \frac{1}{\mu_0}\boldsymbol{B} - \boldsymbol{M}, \tag{1.6}$$

where μ_0 is the permeability of vacuum and $\boldsymbol{M}$ is the magnetization.

The Maxwell's equations define the electromagnetic field generated by charges and currents, but they do not describe how these currents and charges arise. This means, that to solve the Maxwell's equations, so called constitutive (or material) relations are needed, which describe behaviour of materials in an electromagnetic field. These relations are in general tensor equations, because of possible nonlinearities and anisotropy

in materials. However, for linear ($\boldsymbol{P} = \chi_e \boldsymbol{E}$ a $\boldsymbol{M} = \chi_m \boldsymbol{H}$) and isotropic media they have the following form:

$$\boldsymbol{D} = \varepsilon_0 \varepsilon_r \boldsymbol{E} \tag{1.7}$$

$$\boldsymbol{B} = \mu_0 \mu_r \boldsymbol{H} \tag{1.8}$$

$$\boldsymbol{J} = \sigma . \boldsymbol{E}, \tag{1.9}$$

where ε_r and μ_r are the relative permitivity and permeability of the material, respectively, and σ is the specific conductivity.

In the following we will limit ourselves to homogeneous, nonmagnetic media that do not exhibit spatial dispersion. This means, that $\mu_r = 1$ and ε_r and σ are not dependent on position, only on angular frequency ω of the electromagnetic wave.

1.2 Electromagnetic waves

The wave equations can be obtained combining curl equations (1.3) and (1.4), which in vacuum without free charges and currents have the following form:

$$\nabla^2 \boldsymbol{E} - \frac{1}{c} \frac{\partial^2 \boldsymbol{E}}{\partial t^2} = 0, \tag{1.10}$$

$$\nabla^2 \boldsymbol{B} - \frac{1}{c} \frac{\partial^2 \boldsymbol{B}}{\partial t^2} = 0, \tag{1.11}$$

where $c = 1/\sqrt{\mu_0 \varepsilon_0}$ is the vacuum speed of light and operator ∇^2 is defined as:

$$\nabla^2 \equiv \vec{\nabla}(\vec{\nabla}.) - \vec{\nabla} \times \vec{\nabla} \times . \tag{1.12}$$

Because the wave equation can be derived directly from the Maxwell's equations, every solution of Maxwell's equations has to be also a solution to the wave equation. However, the opposite statement is not valid, not every solution to the wave equation satisfies Maxwell equations.

It is known, that the monochromatic plane waves

$$\boldsymbol{E}(\boldsymbol{r}, t) = \boldsymbol{E_0} . exp\left(i(\boldsymbol{k}.\boldsymbol{r} - \omega . t)\right) \tag{1.13}$$

$$\boldsymbol{B}(\boldsymbol{r}, t) = \boldsymbol{B_0} . exp\left(i(\boldsymbol{k}.\boldsymbol{r} - \omega . t)\right) \tag{1.14}$$

are solutions to the wave equation. By substituting (1.13) and (1.14) to the Maxwell's equations is apparent, that if the following conditions are fulfilled:

$$\boldsymbol{k} \perp \boldsymbol{E} \;\; a \; \boldsymbol{k} \times \boldsymbol{E} = \omega \boldsymbol{B}, \tag{1.15}$$

monochromatic plane waves are solutions to the Maxwell's equations.

For homogeneous non conductive media without free charges and currents and the time harmonic electromagnetic field ($\sim \exp(-i\omega t)$), so called Helmholz equations can be

obtained from the Maxwell's equations using similar a procedure as in case of the wave equations:

$$\nabla^2 \boldsymbol{E} + k^2 \boldsymbol{E} = 0 \tag{1.16}$$

$$\nabla^2 \boldsymbol{B} + k^2 \boldsymbol{B} = 0, \tag{1.17}$$

where $k^2 = \mu_0 \mu_r \varepsilon_0 \varepsilon_r \omega^2$, and the propagation speed of the waves is $v = 1/\sqrt{\mu_0 \mu_r \varepsilon_0 \varepsilon_r}$.

In general, the electromagnetic fields are not time harmonic, but they have an arbitrary time dependence. To calculate the time developement of such arbitrary fields Fourier transformed Maxwell's equations are required.

The spectrum $\hat{\mathbf{E}}(\mathbf{r}, \omega)$ of an arbitrary field $\mathbf{E}(\mathbf{r}, \mathrm{t})$ is calculated using the Fourier transform:

$$\widehat{\boldsymbol{E}}(\boldsymbol{r}, \omega) = \frac{1}{2\pi} \int_{-\infty}^{\infty} \boldsymbol{E}(\boldsymbol{r}, t) e^{i\omega t} \, \mathrm{d}t. \tag{1.18}$$

Applying the Fourier transform to the Maxwell's equations gives the following equations:

$$\nabla . \widehat{\boldsymbol{D}} = \hat{\rho}_{ext}(\boldsymbol{r}, \omega) \tag{1.19}$$

$$\nabla . \widehat{\boldsymbol{B}}(\boldsymbol{r}, \omega) = 0 \tag{1.20}$$

$$\nabla \times \widehat{\boldsymbol{E}}(\boldsymbol{r}, \omega) = -i\omega \widehat{\boldsymbol{B}}(\boldsymbol{r}, \omega) \tag{1.21}$$

$$\nabla \times \widehat{\boldsymbol{H}}(\boldsymbol{r}, \omega) = \hat{\boldsymbol{j}}(\boldsymbol{r}, \omega) + \widehat{\boldsymbol{D}}(\boldsymbol{r}, \omega). \tag{1.22}$$

Firstly, the solution for $\hat{\mathbf{E}}(\mathbf{r}, \omega)$ is calculated and the time dependent field is determined as the inverse Fourier transform of $\hat{\mathbf{E}}(\mathbf{r}, \omega)$:

$$\boldsymbol{E}(\boldsymbol{r}, t) = \int_{-\infty}^{\infty} \widehat{\boldsymbol{E}}(\boldsymbol{r}, \omega) e^{-i\omega t} \, d\omega. \tag{1.23}$$

Thus, time dependence of an arbitrary field is Fourier transformed and every spectral component is calculated as a monochromatic field and subsequently inversely transformed to obtain the general time dependence.

1.3 Optical properties of metals

Every environment influences the propagation of electromagnetic waves. In case of the visible light there are many examples observable in every day life supporting this statement. For example, water and glass reflect just a small part of the incident light, the majoritiy of light is transmitted, materials which appear to be black absorb most of the incoming light and metals like silver are shiny and opaque due to effective reflection of the light.

These effects are in fact consequences of optical properties of given materials. For quantitative description of optical properties of materials mostly two quantities are used: complex index of refraction:

$$N = n + ik \tag{1.24}$$

and the complex dielectric function (relative permitivity)

$$\varepsilon = \varepsilon' + i\varepsilon''. \tag{1.25}$$

These quantities are not independent on each other, but are connected through the following formula:

$$N = \sqrt{\varepsilon}\,. \tag{1.26}$$

Consequently, the real and imaginary parts of the index of refraction and dielectric function can be obtained using these quantities:

$$\varepsilon' = n^2 - k^2 \tag{1.27}$$

$$\varepsilon'' = 2nk \tag{1.28}$$

$$n = \left(\frac{\varepsilon'}{2} + \frac{1}{2}\sqrt{\varepsilon' + \varepsilon''}\right)^{\frac{1}{2}} \tag{1.29}$$

$$k = \left(-\frac{\varepsilon'}{2} + \frac{1}{2}\sqrt{\varepsilon' + \varepsilon''}\right)^{\frac{1}{2}}. \tag{1.30}$$

In the following, the optical properties of metals will be discussed using simple models.

1.4 Lorentz model

The Lorentz oscillator model provides the simplest description of the interaction between atoms and an electromagnetic field. It is a classical model based on a concept from mechanics.

The starting point is that electrons are bound to nuclei with a restoring force which is linearly dependent on the displacement from the equilibrium position. This means, that the atoms of a material are represented as harmonic oscillators. The incident field is interacting with the electrons, resulting in a harmonic motion in case of a time harmonic electromagnetic field.

According to this model, taking into account damping as well, the equation of motion for an electron can be expressed as:

$$m\ddot{\boldsymbol{x}} + \gamma\dot{\boldsymbol{x}} + K\boldsymbol{x} = -e\boldsymbol{E}(t), \tag{1.31}$$

where m is the mass of the electron, $\boldsymbol{x}$ is the displacement of the electron from its equilibrium position, K is the restoring constant, γ is the damping coefficient and the time harmonic field can be expressed as:

$$\boldsymbol{E}(t) = \boldsymbol{E_0}.exp(-i\omega t). \tag{1.32}$$

Magnetic forces are usually neglected with respect to electrical forces and radiaton reactions are also neglected. The solution of this differential equation yields the displacement of electrons affected by the time harmonic field:

$$\boldsymbol{x} = -\frac{e/m}{\omega_0^2 - \omega^2 - i\gamma\omega}\boldsymbol{E}. \tag{1.33}$$

where $\omega_0^2 = K/m$ is the resonant frequency of the oscillators. The displacement of electrons towards positive ions induces polarization effects. The magnitude of polarization in unit volume is:

$$\boldsymbol{P} = -ne\boldsymbol{x} = \frac{ne^2}{m(\omega_0^2 - \omega^2 - i\gamma\omega)}\boldsymbol{E}, \tag{1.34}$$

where *n* is the density of electrons. By substituing (1.34) into (1.5) we obtain:

$$\boldsymbol{D} = \varepsilon_0\boldsymbol{E} + \frac{ne^2}{m(\omega_0^2 - \omega^2 - i\gamma\omega)}\boldsymbol{E} = \varepsilon_0\left(1 + \frac{\omega_p^2}{\omega_0^2 - \omega^2 - i\gamma\omega}\right)\boldsymbol{E}, \tag{1.35}$$

where $\omega_p^2 = \frac{ne^2}{m\varepsilon_0}$ is the plasma frequency of the free electron gas [2]. The dielectric function can be obtained by comparsion of (1.7) and (1.35):

$$\varepsilon(\omega) = 1 + \frac{\omega_p^2}{\omega_0^2 - \omega^2 - i\gamma\omega}. \tag{1.36}$$

The real and imaginary parts of the dielectric function have the following form:

$$\varepsilon'(\omega) = 1 + \frac{\omega_p^2(\omega_0^2 - \omega^2)}{(\omega_0^2 - \omega^2)^2 + \gamma^2\omega^2} \tag{1.37}$$

$$\varepsilon''(\omega) = \frac{\omega_p^2\gamma\omega}{(\omega_0^2 - \omega^2)^2 + \gamma^2\omega^2}. \tag{1.38}$$

Altough the Lorentz model is a purely classical model, it gives a good basic insight into the problem of atom-field interactions. The model becomes even more useful if more types of harmonic oscillators (with different resonant frequecies) are considered ([3] pp.244).

In the following section, the particular situation of metals will be investigated (the charge moves freely within the material).

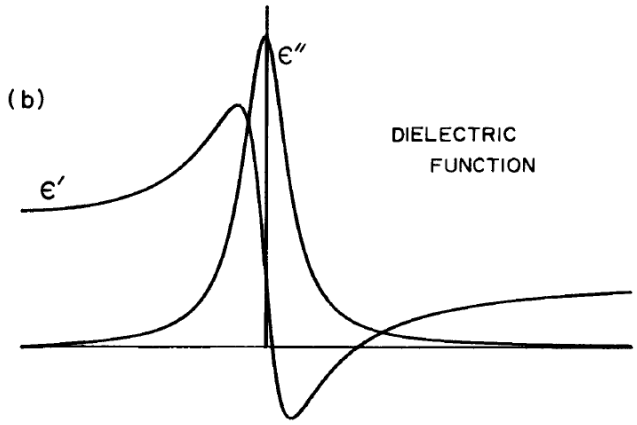

Figure 1.1 Frequency dependence of the real and imaginary parts of the dielectric function according to the Lorentz model. Picture taken from [3] pp. 230.

1.5 Drude model

Paul Drude proposed his model in 1900 to explain conduction properties of metals [4]. The model was further advanced by Arnold Sommerfelder in 1933 by taking into account quantum mechanical principles. The Drude model is in fact an asymptotic case of the Lorentz model but from the chronological point of view it foregoes the Lorentz model.

The model is based on the idea, that electrons inside metals create a free electrons gas. This means electrons can freely move inside metals without resistance, without interaction with each other and they are not bounded to the positive ions of the crystal. Furthermore, electrons undergo elastic collisions with the heavier positive ions with frequency $\gamma = 1/\tau$, where τ is the average time between collisions (relaxation time).

When an external time harmonic electric field is considered, the equation of motion of electrons has the following form:

$$m\ddot{\boldsymbol{x}} + m\gamma\dot{\boldsymbol{x}} = -e\boldsymbol{E}. \tag{1.39}$$

The solution of this differential equation is:

$$\boldsymbol{x}(t) = \frac{e}{m(\omega^2 + i\gamma\omega)}\boldsymbol{E}(t). \tag{1.40}$$

The dielectric function can be obtained by the same procedure, as in case of the Lorentz model:

$$\varepsilon(\omega) = 1 - \frac{\omega_p^2}{(\omega^2 + i\gamma\omega)}. \tag{1.41}$$

The real and imaginary parts of the dielectric function have the following form:

$$\varepsilon'(\omega) = 1 - \frac{\omega_p^2\tau^2}{(1 + \omega^2\tau^2)} \tag{1.42}$$

$$\varepsilon''(\omega) = \frac{\omega_p^2 \tau^2}{\omega(1+\omega^2\tau^2)} \tag{1.43}$$

At high frequency values (with respect to γ) close to the plasma frequency, where $\omega\tau \gg 1$, the dielectric function is predominantly real:

$$\varepsilon(\omega) = 1 - \frac{\omega_p^2}{\omega^2}, \tag{1.44}$$

which can be taken as the dielectric function of the undamped free electron plasma [5].

It is imprtant to note, that the Drude model itself does not precisely describe the optical properties of all metals, because not only free but also bounded electrons are present in the atoms. The free electrons can be treated according to the Drude model, but bound-electrons have to be treated by means of Lorentz oscillators to calculate the dielectric function of real metals a combination of Drude and Lorentz model is required.

1.6 Kramers-Kronig relations

The Kramers-Kronig relations connect the real and imaginary parts of dielectric function and provide fundamental constrains for the linear frequency-dependent response of a system to an external perturbation [6]. These integral relations are often used to find the complex refractive index of a medium from a measured absorption, reflection or transmission spectrum or to calculate the real part from the imaginary counterpart (or vice versa) of the dielectric function.

The Kramers-Kronig relations for the dielectric function have the following form:

$$\varepsilon'(\omega) = 1 + \frac{2}{\pi} P \int_0^\infty \frac{\Omega \varepsilon''(\Omega)}{\Omega^2 - \omega^2} \mathrm{d}\Omega \tag{1.45}$$

$$\varepsilon''(\omega) = -\frac{2\omega}{\pi} P \int_0^\infty \frac{\varepsilon'(\Omega) - 1}{\Omega^2 - \omega^2} \mathrm{d}\Omega, \tag{1.46}$$

where *P* denotes the Cauchy principal value.

The derivation of the Kramers-Kronig relations is based on the basic physical principle of causality and on Cauchy's residue theorem. In the case of the interaction of an electromagnetic wave with a medium, the causality implies that the medium will respond to an external perturbation (incident wave) only after its occurrence (incidence). In the spectral region of the visible light, the response of the medium can be observed as the polarization of electrons. Kramers and Kronig realized, that knowing over the full spectral range either the real or the imaginary part of the complex refractive index it is possible to reconstruct the full refractive index. The detailed derivation can be found in [7] pp. 306-312.

2 Surface plasmon polaritons

The subject of this chapter is to define the basic notions used in the field of plasmonics and to derivate the existence and basic properties of surface plasmon polaritons.

As mentioned in the previous chapter, plasmons are the oscillation quanta of the free electron gas in metals. When these oscillations occur at the metal suface we talk about surface plasmons and when they occur in the bulk we talk about volume plasmons.

Surface plasmon polaritons (SPP) are quasiparticles arising via coupling of electromagnetic field to oscillations of the free electron gas. The resulting electromagnetic surface waves travel at a metal-dielectric interface and they are strongly confined to the interface and exhibit an exponential decay perpendicular to the interface.

For the simplicity, in the following text instead of the correct term surface plasmon polariton, shortly just the term surface plasmon or SPP will be mostly used.

2.1 Surface plasmon polaritons at metal/insulator interfaces

The existence of surcface plasmons can be derived by solving the Maxwell's equations without free charges and currents at a planar interface. The solutions are waves coupled to the surface. The first assumptions will be that the waves are time harmonic ($\sim\exp(-i\omega t)$), propagate in the x direction, they are homogenous along the y direction and the interface is at the $z = 0$ coordinate, as it is shown in the Figure 2.1.

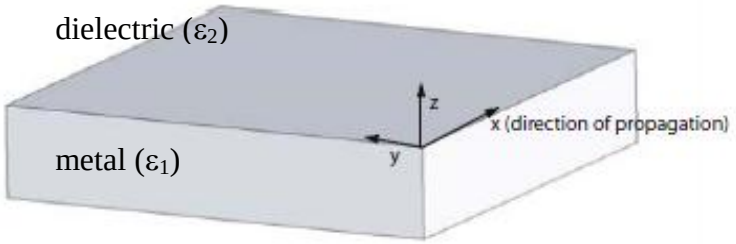

Figure 2.1. Planar metal-dielectric interface. Picture taken from [5].

Furthermore, the propagating waves expected to have the following expression:

$$\boldsymbol{E}(x,y,z) = \boldsymbol{E}(z)e^{i\beta x}, \tag{2.1}$$

where β is the propagation constant of the waves in the x direction. Inserting this expression to the Helmholtz equation yields:

$$\frac{\partial^2 \boldsymbol{E}}{\partial z^2} - (k_0^2\varepsilon - \beta^2)\boldsymbol{E} = 0, \tag{2.2}$$

where $k_0 = \omega/c$. A similar wave equation can be obtained for the magnetic field $\boldsymbol{H}$.

To obtain the spatial wave profile from these wave equations, it is neccesary to have explicit expressions for the intensity of the electric ($\boldsymbol{E}$) and magnetic ($\boldsymbol{H}$) field. These expressions can be obtained from the Maxwell's equations. Provided, that the fields have a harmonic time dependence $\left(\frac{\partial}{\partial t} = -i\omega\right)$, the waves propagate in the x direction $\left(\frac{\partial}{\partial x} = i\beta\right)$ and are homogeneous in the y direction $\left(\frac{\partial}{\partial y} = 0\right)$, the curl equations yield the following set of coupled equations:

$$\frac{\partial E_y}{\partial z} = -i\omega\mu_0 H_x \tag{2.3}$$

$$\frac{\partial E_x}{\partial z} - i\beta E_z = i\omega\mu_0 H_y \tag{2.4}$$

$$i\beta E_y = i\omega\mu_0 H_z \tag{2.5}$$

$$\frac{\partial H_y}{\partial z} = i\omega\varepsilon_0\varepsilon E_x \tag{2.6}$$

$$\frac{\partial H_x}{\partial z} - i\beta H_z = -i\omega\varepsilon_0\varepsilon E_y \tag{2.7}$$

$$i\beta H_y = -i\omega\varepsilon_0\varepsilon E_z. \tag{2.8}$$

These equations can be divided into two independent sets of equations. The first represents the transveral magnetic (TM) modes, where only the E_x, E_z and H_y components of the field are nonzero:

$$E_x = -\frac{i}{\omega\varepsilon\varepsilon_0}\frac{\partial H_y}{\partial z} \tag{2.9}$$

$$E_z = -\frac{\beta}{\omega\varepsilon\varepsilon_0}H_y. \tag{2.10}$$

By substituing these two equations into (2.4) we obtain the wave equation for the H_y component in the TM modes:

$$\frac{\partial^2 H_y}{\partial z^2} - (k_0^2 \varepsilon - \beta^2) H_y = 0. \tag{2.11}$$

The seconds set corresponds to the transversal electric (TE) modes, where only H_x, H_z and E_y components of the field are nonzero:

$$H_x = \frac{i}{\omega \mu_0} \frac{\partial E_y}{\partial z} \tag{2.12}$$

$$H_z = \frac{\beta}{\omega \mu_0} E_y. \tag{2.13}$$

By substituing these two equations into (2.7) we obtain the wave equation for the TM modes:

$$\frac{\partial^2 E_y}{\partial z^2} - (k_0^2 \varepsilon - \beta^2) E_y = 0. \tag{2.14}$$

For the planar geometry of the interface (see Figure 2.1) the TM solutions have the following form:

$$H_y(z) = A_2 e^{i\beta x} e^{-k_2 z} \tag{2.15}$$

$$E_x(z) = i A_2 \frac{1}{\omega \varepsilon_0 \varepsilon_2} k_2 e^{i\beta x} e^{-k_2 z} \tag{2.16}$$

$$E_z(z) = -A_2 \frac{\beta}{\omega \varepsilon_0 \varepsilon_2} e^{i\beta x} e^{-k_2 z} \tag{2.17}$$

for z > 0 and

$$H_y(z) = A_1 e^{i\beta x} e^{k_1 z} \tag{2.18}$$

$$E_x(z) = -i A_1 \frac{1}{\omega \varepsilon_0 \varepsilon_1} k_1 e^{i\beta x} e^{k_1 z} \tag{2.19}$$

$$E_z(z) = -A_1 \frac{\beta}{\omega \varepsilon_0 \varepsilon_1} e^{i\beta x} e^{k_1 z} \tag{2.20}$$

for z < 0.

The parameter k_1 is the component of the wave vector perpendicular to the interface in the metal which can be expressed as:

$$k_1^2 = \beta^2 - k_0^2 \varepsilon_1 \tag{2.21}$$

and k_2 is the component of the wave vector perpendicular to the interface in the dielectric

$$k_2^2 = \beta^2 - k_0^2 \varepsilon_2. \tag{2.22}$$

Furthermore, ε_2 is the dielectric constant of the dielectric and ε_1 is the complex dielectric function of the metal.

From the boundary conditions (continuity of E_x and H_y) at the interface we obtain $A_1 = A_2$ and

$$\frac{k_2}{k_1} = -\frac{\varepsilon_2}{\varepsilon_1}. \tag{2.23}$$

Combining (2.23) and equations (2.21)-(2.22) yields the main result of this computation, which is the dispersion relation of the SPPs propagating at the planar interface between a metal and a dielectric:

$$\beta = k_x = k_0 \sqrt{\frac{\varepsilon_1 \varepsilon_2}{\varepsilon_1 + \varepsilon_2}}. \tag{2.24}$$

The TE solutions are formally very similar to the TM solutions:

$$E_y(z) = A_2 e^{i\beta x} e^{-k_2 z} \tag{2.25}$$

$$H_x(z) = -iA_2 \frac{1}{\omega \mu_0} k_2 e^{i\beta x} e^{-k_2 z} \tag{2.26}$$

$$H_z(z) = A_2 \frac{\beta}{\omega \mu_0} e^{i\beta x} e^{-k_2 z} \tag{2.27}$$

for z > 0 and

$$E_y(z) = A_1 e^{i\beta x} e^{k_1 z} \tag{2.28}$$

$$H_x(z) = iA_1 \frac{1}{\omega \mu_0} k_1 e^{i\beta x} e^{k_1 z} \tag{2.29}$$

$$H_z(z) = A_1 \frac{\beta}{\omega \mu_0} e^{i\beta x} e^{k_1 z} \tag{2.30}$$

for z < 0. Continuity of E_y and H_x at the interface yields conditions $A_1 = A_2$ and:

$$A_1(k_1 + k_2) = 0. \tag{2.31}$$

This condition is only fulfilled if $A_1 = 0$ due to the evnanescent character of the waves ($Re[k_1]$ and $Re[k_2]$ has to be positive). Thus, the solution doesn‘t exist for the TE polarization of the surface waves, only for the TM polarization.

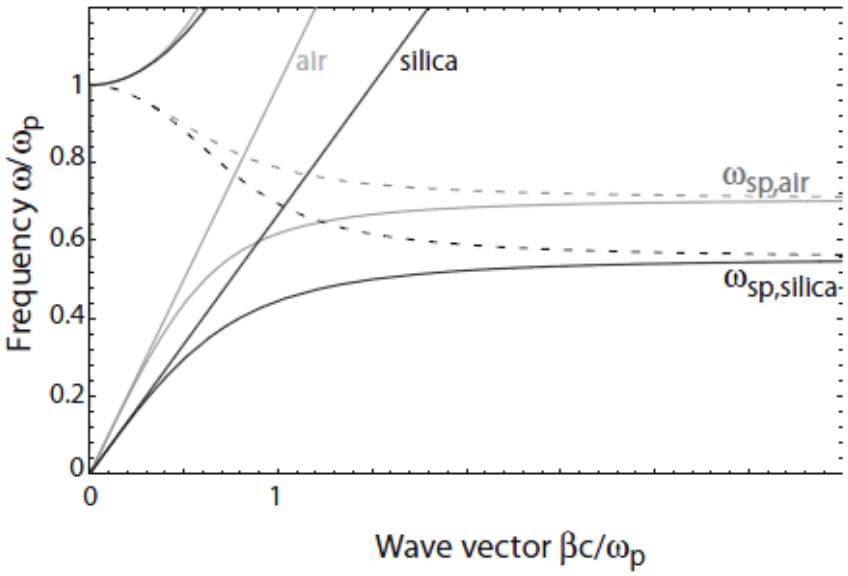

Figure 2.2. Dispersion relation of SPPs at the interface between a Drude metal with negligible collison frequency and air (grey curve) or silica (black curve) normalized to the plasma frequency ω_p. Solid curve- real part of β, dashed curve- imaginary part of β. Picture taken from [5].

Figure 2.2 shows both the real (solid curves) and imaginary (dashed curves) part of the wave vector β for an interface between an ideal metal (negligible damping) and air or silica. It is apparent from this figure, that the wave vector of SPPs is always bigger than the wave vector of light with the same frequency. This results in the fact that SPPs cannot be excited by direct impact of light on the interface and special wave vector (momentum) matching techniques are required to excite SPPs at planar interfaces (see at [5] Chapter 3). However, at low frequencies (mid-infrared or lower) the wave vector of SPPs is close to the wave vector of light and SPPs can be excited via grazing-incidence light field. These SPPs are known as the Sommerfeld- Zenneck waves [5].

In the opposite regime, the propagation constant of SPPs diverges at the characteristic surface plasmon frequency:

$$\omega_{sp} = \frac{1}{\sqrt{1+\varepsilon_2}}. \tag{2.32}$$

This relationship can be obtained by inserting (1.44) into (2.24) for $\beta = \infty$. Between the surface plasmon frequency and plasma frequency exists a frequency gap, where β is purely imaginary (see Figure 2.2), thus at these frequencies SPP propagation is prohibited. At frequencies higher than the plasma frequency the metal becomes transparent (curves lying to the left of the light lines).

The discussion above is valid only for ideal conductors, where $Im(\varepsilon_2)=0$. For real metals the travelling waves are damped, so β has a finite limit at the surface plasmon frequency. Also for real metals doesn't exists a prohibited frequency region between ω_{sp} and ω_p.

3 Localised surface plasmons

In the previous chapter the basic propagating excitations of surface plasmon polaritons were introduced. The subject of this chapter is devoted to the localized surface plasmons, which represent a special case of SPPs.

The localised surface plasmons (LSPs) are non-propagating excitations arising from coupling of the electromagnetic field to the oscillations of conduction electrons of metal nanoparticles or similar nanostructures (e.g. antennas). The electron oscillations are limited by the size and the shape of the particles leading to localised and non- propagating nature of these surface plasmon polaritons.

LSPs have an advantage in contrast to the SPPs, that due to the curved particle surface they can be excited without using special techniques, just by direct light illumination. The limted size and curved surface allows also resonances of LSPs leading to a strongly enhanced elemectromagnetic field in proximity of the particles (nanostructures).

In the following the conditions of LSP resonance on a metallic sphere and the enhanced field will be investigated using two different analytical methods: the quasi-static approximation and Mie theory.

3.1 Quasi-static approximation

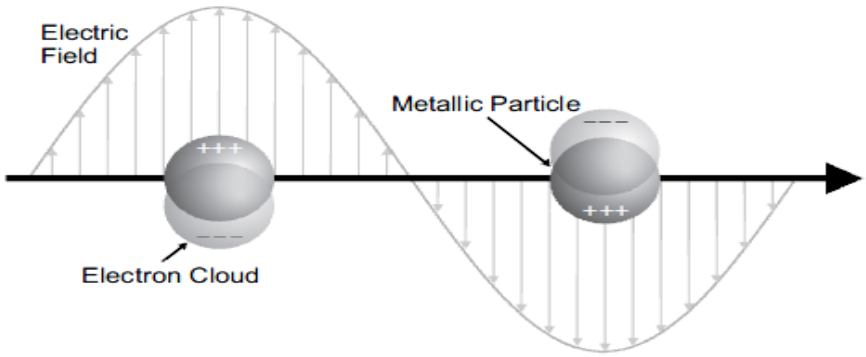

Figure 3.1. Metal sphere in electromagnetic field. Picture taken from [8].

The quasi-static approximation is a useful and accurate method for computing resonance frequency and enhanced field in case of very small spherical particles. When the sphere diameter is much smaller than the wavelength of the incident light ($\lambda >> d$), the phase of the oscillating field can be considered as a constant in the whole volume of the sphere (i.e. the field retardation is neglected). Thus, the spatial charge distribution can be solved as an electrostatic problem and the time dependence can be added afterwards.

Hence, the starting point of calculation is the problem of a metal sphere in an electrostatic field [9].

A homogenous isotropic metal sphere placed in the origion of the coordinate system and having a dielectric function $\varepsilon(\omega)$ is located in the homogeneous electrostatic field $\boldsymbol{E} = E_0\hat{\boldsymbol{z}}$ (see Figure 3.2). The sphere is surrounded by a homogeneous, non-absorbing medium with the dielectric constant ε_m. First, the potential distribution is determined using the Laplace equation $\nabla^2\Phi = 0$ and subsequently the corresponding electric field by the relation $\boldsymbol{E} = -\nabla\Phi$.

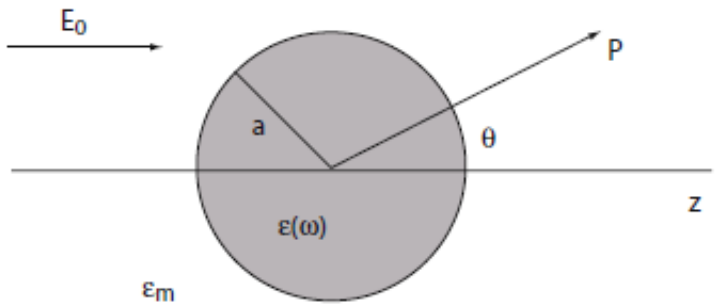

Figure 3.2. Geometry of the problem. Picture taken from [5].

Due to the spherical symmetry the Laplace equation is solved in spherical coordinates (r,ϕ,θ):

$$\frac{1}{r}\frac{\partial^2}{\partial r^2}(r\Phi) + \frac{1}{r^2 sin\theta}\frac{\partial}{\partial\theta}\left(\sin\theta\frac{\partial\Phi}{\partial\theta}\right) + \frac{1}{r^2\sin^2\theta}\frac{\partial^2\Phi}{\partial\phi^2} = 0. \qquad (3.1)$$

The solution is expected in the form of:

$$\Phi(r,\theta,\phi) = \frac{U(r)}{r}P(\theta)F(\phi). \qquad (3.2)$$

Substitution of (3.2) to (3.1) yields after small modification:

$$r^2\sin^2\theta\left(\frac{U''}{U} + \frac{1}{Pr^2 sin\theta}\frac{\partial}{\partial\theta}(\sin(\theta)\,P')\right) = -\frac{F''}{F}. \qquad (3.3)$$

The equality has to be fulfilled for any r, ϕ and θ, yieldig thus both sides of the equation equal a constant, denoted as m^2. Equation (3.3) fragments then to two equations:

$$F'' + m^2F = 0 \qquad (3.4)$$

$$r^2 \frac{U''}{U} = -\frac{1}{Psin\theta}\frac{\partial}{\partial\theta}(\sin\theta\, P') + \frac{m^2}{\sin^2\theta}. \tag{3.5}$$

The left side of the equation (3.5) is dependent only on *r* and the right side only on θ. It is possible again only when both sides equal a constant value. In that case the constant is introduced as *l(l+1)*.

$$U'' - \frac{l(l+1)}{r^2}U = 0 \tag{3.6}$$

$$\frac{1}{\sin\theta}\frac{\partial}{\partial\theta}(\sin\theta\, P') + \left(l(l+1) - \frac{m^2}{\sin^2\theta}\right)P = 0. \tag{3.7}$$

Using assumption (3.2) it was possible to transfer the partial differential equation (3.1) into three ordinary differential equations (3.4), (3.6) and (3.7) with known analytical solution. Equation (3.4) has analytical solution:

$$F(\phi) = \exp(\pm im\phi), \tag{3.8}$$

where *m* is comlex constant. The symmetry of the problem implies that the condition $F(\phi) = F(\phi+2\pi)$ has to be fulfilled and it yields that *m* can take only values *m* = 0, 1, 2 ... Furthermore, the symmetry also implies independence on the azimuthal angle, which leads to *m = 0* and

$$F(\phi) = 1. \tag{3.9}$$

The solution to (3.6) has a form of:

$$U(r) = A_l r^l + B_l r^{-l-1}, \tag{3.10}$$

where in general A_l a B_l are complex constants. The meaning of index *l* will be discussed later. Using the substitution $x = cos\theta$ and relationship *m = 0*, the so called Legendre equation can be obtained from the equation (3.7):

$$\frac{d}{dx}\left((1-x^2)\frac{dP}{dx}\right) + l(l+1)P = 0. \tag{3.11}$$

The solutions to this equation are the Legendre polynomials:

$$P_l(x) = \frac{1}{2^l l!}\frac{d^l}{dx^l}(x^2-1)^l, \tag{3.12}$$

where *l* = 0,1,2... is the degree of polynomials.

The general solution is given by the linear combination of products of $U_l(r)$ and $P_l(\theta)$:

$$\Phi(r,\theta) = \sum_{l=0}^{\infty}(A_l r^l + B_l r^{-l-1})\, P_l(\cos\theta). \tag{3.13}$$

The constants *A* and *B* will be determined using boundary conditions on the surface of the sphere and at very large distances from the sphere. These constants are different inside

and outside the sphere, therefore the solution is diveded into two parts: the potential outside the sphere is denoted $\Phi^{\mathrm{e}}(r,\theta)$ and the potential inside as $\Phi^{\mathrm{i}}(r,\theta)$.

$$\Phi^{\mathrm{e}}(r,\theta) = \sum_{l=0}^{\infty} (A_l r^l + B_l r^{-l-1})\, P_l(\cos\theta) \tag{3.14}$$

$$\Phi^{\mathrm{i}}(r,\theta) = \sum_{l=0}^{\infty} (C_l r^l + D_l r^{-l-1})\, P_l(\cos\theta). \tag{3.15}$$

The magnitude of electric field intensity of the electric field at very large distances from the sphere has to be E_0, which yields the condition for the potential outside the sphere:

$$\Phi|_{r\to\infty} = -E_0 r\cos\theta. \tag{3.16}$$

It follows than, that $A_1 = -E_0$ and $A_l = 0$ for $l \neq 1$. Furthermore, the potential can not diverge at the center of the sphere (for $r = 0$), which results in $D_l = 0$ for all l. The remaining unkown constants are determined using continuity conditions of tangential component of $\boldsymbol{E}$ and perpendicular component of $\boldsymbol{D}$. The final form of the potential is:

$$\Phi^{\mathrm{e}}(r,\theta) = -E_0 r\cos\theta + \frac{\varepsilon-\varepsilon_m}{\varepsilon+2\varepsilon_m} E_0 a^3 \frac{cos\theta}{r^2} \tag{3.17}$$

$$\Phi^{\mathrm{i}}(r,\theta) = -\frac{3\varepsilon_m}{\varepsilon+2\varepsilon_m} E_0 r\cos\theta. \tag{3.18}$$

It is apparent from equation (3.17) that the field outside the sphere is a superposition of two fields: a homogenous field in which the sphere is placed and the scattered field from a dipole located in the center of the sphere. By introducing a dipole moment

$$\boldsymbol{p} = 4\pi\varepsilon_0\varepsilon_m a^3 \frac{\varepsilon-\varepsilon_m}{\varepsilon+2\varepsilon_m}\boldsymbol{E_0}, \tag{3.19}$$

Eq. (3.17) is amending to:

$$\Phi^{\mathrm{e}}(r,\theta) = -E_0 r\cos\theta + \frac{\boldsymbol{p}.\boldsymbol{r}}{4\pi\varepsilon_0\varepsilon_m r^3}. \tag{3.20}$$

Furthermore, the polarizability α can be introduced using relationship $\boldsymbol{p} = \varepsilon_0\varepsilon_m\alpha\boldsymbol{E_0}$ as

$$\alpha = 4\pi a^3 \frac{\varepsilon-\varepsilon_m}{\varepsilon+2\varepsilon_m}. \tag{3.21}$$

Equation (3.21) expresses the complex polarizability of the spehere according to the quasi-static approximation. It is important to note, that, if the denominator $|\varepsilon+2\varepsilon_m|$ vanishes, the resonant enhancement of polarizability occures. When $Im[\varepsilon]$ is negligible, the resonant condition is fulfilled for:

$$Re[\varepsilon] = -2\varepsilon_m. \tag{3.22}$$

This relationship is known as the Fröhlich condition and for Drude-metal spheres in vacuum is fulfilled at frequnecy:

$$\omega_0 = \frac{\omega_p}{\sqrt{3}}. \tag{3.23}$$

The distribution of electric field can be obtained from $\boldsymbol{E} = -\nabla\Phi$, which yields:

$$\boldsymbol{E^i} = \frac{3\varepsilon_m}{\varepsilon + 2\varepsilon_m}\boldsymbol{E_0} \tag{3.24}$$

$$\boldsymbol{E^e} = \boldsymbol{E_0} + \frac{3\boldsymbol{n}(\boldsymbol{n}.\boldsymbol{p}) - \boldsymbol{p}}{4\pi\varepsilon_0\varepsilon_m}\frac{1}{r^3}, \tag{3.25}$$

where $\boldsymbol{n}$ is the unit vector in the direction of the point of interest. It is apparent, that resonance in polarizability implies resonant enhancement of the electric field outside and inside the sphere. This resonance is called the localised surface plasmon resonance. From the previous considerations it is also apparent that in the quasi-static approximation the sphere acts like an ideal dipole.

Up to this point the problem was treaed purely electrostaticly and the field distribution at a given moment was obtained. In the following the time dependence and the magnetic field are added to the solution.

A monochromatic plane wave is impinging on the sphere, which means the incident field is time harmonic:

$$\boldsymbol{E}(t) = \boldsymbol{E_0} exp(-i\omega t). \tag{3.26}$$

The oscillating electric field induces oscillation in the sphere's dipole moment:

$$\boldsymbol{p}(t) = \varepsilon_0\varepsilon_m\alpha\boldsymbol{E_0} exp(-i\omega t). \tag{3.27}$$

It is known, that the oscillating dipole is irradiating electromagnetic waves and the radiated field can be described with the following equations [7]:

$$\boldsymbol{H} = \frac{ck^2}{4\pi}(\boldsymbol{n}\times\boldsymbol{p})\frac{e^{ikr}}{r}\left(1 - \frac{1}{ikr}\right) \tag{3.28}$$

$$\boldsymbol{E} = \frac{1}{4\pi\varepsilon_0\varepsilon_m}\left[k^2(\boldsymbol{n}\times\boldsymbol{p})\times\boldsymbol{n}\frac{e^{ikr}}{r} + (3\boldsymbol{n}(\boldsymbol{n}.\boldsymbol{p}) - \boldsymbol{p})\left(\frac{1}{r^3} - \frac{ik}{r^2}\right)e^{ikr}\right]. \tag{3.29}$$

Surface plasmons are confined to the surface of the metal, therefore more interesting is the expression of the electromagnetic field in the near-field zone close to the sphere‘s surface. By taking into account that in the near field, where *k.r << 1* is valid, equations (3.28) and (3.29) are simplified to:

$$\boldsymbol{H} = \frac{i\omega}{4\pi}(\boldsymbol{n}\times\boldsymbol{p})\frac{1}{r^2} \tag{3.30}$$

$$\boldsymbol{E} = \frac{3\boldsymbol{n}(\boldsymbol{n}.\boldsymbol{p}) - \boldsymbol{p}}{4\pi\varepsilon_0\varepsilon_m}\frac{1}{r^3}. \tag{3.31}$$

To summarize, in the quasi-static approximation the sphere scatters the incident plane wave, which can be represented as a radiation by an ideal point dipole. It is important to note, that the localised surface plasmons arise naturally from this scattering

on a small sphere. When the Fröhlich condition is met, the dipole associated resonance of the localised surface plasmon occurs. This condition is fulfilled for Drude-metal spheres placed in vacuum at frequency $\omega_0 = \omega_p/\sqrt{3}$.

3.2 Mie theory

When the size of the particle is not negligible in comparison to the wavelength of the incident wave, the quasi-static approximation is not giving correct results. The phase shift of the wave along the particle must be considered. In this case it is suitable to use the Mie theory, which uses a correct electrodynamic approach.

Gustav Mie, a German physicist, published in 1908 analytical solutions to the Maxwell's equations for absorption and scattering of light on spherical particles. His solution is pivoted on the expression of the scattered field and the field inside the particles using so called normal modes which are evaluated via vector harmonics. In the following the basic ideas and the results of this theory are represented. The detailed description of the Mie theory can be found in [3] pp. 80-111.

Using a scalar function ψ and pilot vector $\boldsymbol{r}$ vector functions $\boldsymbol{M}$ and $\boldsymbol{N}$ are defined in the following way:

$$\boldsymbol{M} = \nabla \times \boldsymbol{r}\psi \quad \text{and} \quad \boldsymbol{N} = \nabla \times \boldsymbol{M}/\mathrm{k}. \tag{3.32}$$

By means of vector identities it is possible to prove the validity of equations:

$$\nabla^2\mathbf{M} + \mathrm{k}^2\mathbf{M} = \nabla \times [\mathbf{r}(\Delta\psi + \mathrm{k}^2\psi)]. \tag{3.33}$$

If the function ψ fulfills the scalar wave equation the right side of the equation equals zero, resulting in the fact that $\boldsymbol{M}$ fulfills the vector wave equation. The same condition is valid for the vector $\boldsymbol{N}$. Between the vectors $\boldsymbol{M}$, $\boldsymbol{N}$ and $\boldsymbol{B}$, $\boldsymbol{E}$ exists homomorfism, because both pairs have the necessary properties to describe electromagnetic field.

The introduction of vectors $\boldsymbol{M}$ and $\boldsymbol{N}$ simplifies the scattering problem. It is not neccesary to solve two vector wave equations to obtain the electromagnetic field, just the scalar wave equation for ψ is needed. If the functions ψ and $\boldsymbol{r}$ are determined, using equations (3.32) it is easy to obtain vectors $\boldsymbol{M}$ and $\boldsymbol{N}$.

Because of the symmetry of the problem the scalar wave equation is solved in spherical coordinates and in this particular case the pilot vector is directly the polar vector $\boldsymbol{r}$ (for that reason it was denoted as $\boldsymbol{r}$ fom the beginning).

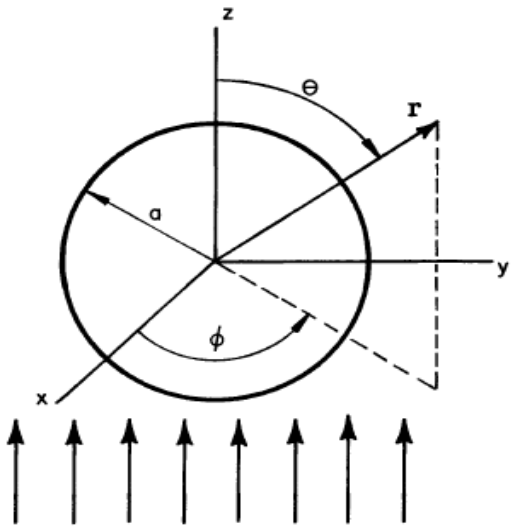

Figure. 3.3. Geometric configuration of the problem. Picture taken from [3].

The solutions to the wave equation are functions:

$$\psi_{emn} = cos(m\phi).P_n^m(cos\theta)z_n(kr) \tag{3.34}$$

$$\psi_{omn} = sin(m\phi).P_n^m(cos\theta)z_n(kr). \tag{3.35}$$

The indexes *e, o* express the parity (even and odd), indexes *m* a *n* the order and degree of the Legendre polynomials, respectively, and functions $z_n(kr)$ are the spherical Bessel functions. The so called normal modes can be obtained by introduction of the wave functions to (3.32):

$$\boldsymbol{M_{emn}} = \nabla \times \boldsymbol{r}\psi_{emn} \quad \boldsymbol{M_{omn}} = \nabla \times \boldsymbol{r}\psi_{omn} \tag{3.36}$$

$$\boldsymbol{N_{emn}} = \nabla \times \boldsymbol{M_{emn}}/k \quad \boldsymbol{N_{omn}} = \nabla \times \boldsymbol{M_{omn}}/k. \tag{3.37}$$

It can be shown that these vectors are mutually ortogonal and since the superposition principle is valid the incident wave and the field inside and outside the sphere can be expressed as an infinite series of the normal modes.

The field inside the sphere is:

$$\boldsymbol{E_1} = E_0 \sum_{n=1}^{\infty} i^n \frac{2n+1}{n(n+1)} (c_n \boldsymbol{M}_{o1n} - i d_n \boldsymbol{N}_{e1n}) \tag{3.38}$$

$$\boldsymbol{H_1} = \frac{-k_1}{\omega \mu_1} E_0 \sum_{n=1}^{\infty} i^n \frac{2n+1}{n(n+1)} (d_n \boldsymbol{M}_{e1n} + i c_n \boldsymbol{N}_{o1n}) \tag{3.39}$$

and the scattered field can be expressed as:

$$\boldsymbol{E_s} = E_0 \sum_{n=1}^{\infty} i^n \frac{2n+1}{n(n+1)} (i a_n \boldsymbol{N}_{e1n} - b_n \boldsymbol{M}_{o1n}) \tag{3.40}$$

$$\boldsymbol{H_s} = \frac{-k}{\omega\mu} E_0 \sum_{n=1}^{\infty} i^n \frac{2n+1}{n(n+1)} (i b_n \boldsymbol{N}_{o1n} + a_n \boldsymbol{M}_{e1n}). \tag{3.41}$$

where k_1 and k are the magnitudes of the wave vectors of the incident wave inside and outside the sphere, respectively, and a_n, b_n, c_n, d_n are complex coefficients which can be obtained from boundary conditions at the metal-dielectric interface. In the simplified form the coefficients a_n, b_n have the following expression:

$$a_n = \frac{m\psi_n(mx)\psi_n'(x) - \psi_n(x)\psi_n'(mx)}{m\psi_n(mx)\xi_n'(x) - \xi_n(x)\psi_n'(mx)} \tag{3.42}$$

$$b_n = \frac{\psi_n(mx)\psi_n'(x) - m\psi_n(x)\psi_n'(mx)}{\psi_n(mx)\xi_n'(x) - m\xi_n(x)\psi_n'(mx)}. \tag{3.43}$$

The symbol m denotes the relative index of refraction with respect to the surrounding medium, x is the so called size factor defined as a product of the magnitude of the wave vector k and the sphere diameter a. Furthemore, the functions ψ_n and ξ_n are the Riccati-Bessel functions. The prime indicates differentiation with respect to the function's argument.

Figure 3.4 shows the field distibution of the individual normal modes (only one from the coefficients a_n and b_n is nonzero) on the surface of an imaginary sphere, which is concentric with the particle but has a bigger diameter. When only the coefficients a_n are non-zero, we talk about transversal magnetic modes, because the radial component of the vector $\boldsymbol{H}$ equals zero. When the coefficients b_n are non-zero, we talk about transversal electric mode, because in that case the vector $\boldsymbol{E}$ has no radial component.

For the small spheres ($x \to 0$) the coefficient a_n goes to infinity, when the denominator of the equation (3.42) vanishes. However, the denominator vanishes only for complex frequencies (so called virtual frequencies). For the real frequencies close to the magnitudes of these virtual frequencies the coefficients a_n are very large. The normal modes at these frequencies are the so called surface modes and with an increasing order of the normal modes the electric field inside the sphere is localized closer to the surface (expression for coefficient d_n has the same denominator as the expression for a_n so according to (3.38) the dominant term inside the sphere is $\boldsymbol{N}_{e1n}$, which has the following radial dependence: $\boldsymbol{N}_{e1n}(r) \sim r^{n-1}$).

For the very small spheres only the lowest order surface mode is dominant (coefficient a_1 is dominant). That means, the lowest order surface mode according to the Mie theory has to be equivalent to the quasi-static approximation. From Figure 3.4 it is apparent that the lowest order surface mode generates a dipole-like field, which is in agreement with the quasi-static approximation. Also the Fröhlich condition can be obtained from the Mie theory for $a_1 \to \infty$ ([3] pp. 340-341).

The advantage of the Mie theory is that it is suitable for computing the electromagnetic field inside and outside spherical particles with an arbitrary diameter. The theory was further developed for computing absorption and scattering properties of particles with ellipsoidal or cylindrical shapes. Introduction of the absorption, scattering and extinction cross sections are also very useful tools for characterizing the scattered far field ([3] pp 101-118). Therefore, the Mie theory is mostly used in the field of meteorology for study of many optical problems as cloud scattering etc.

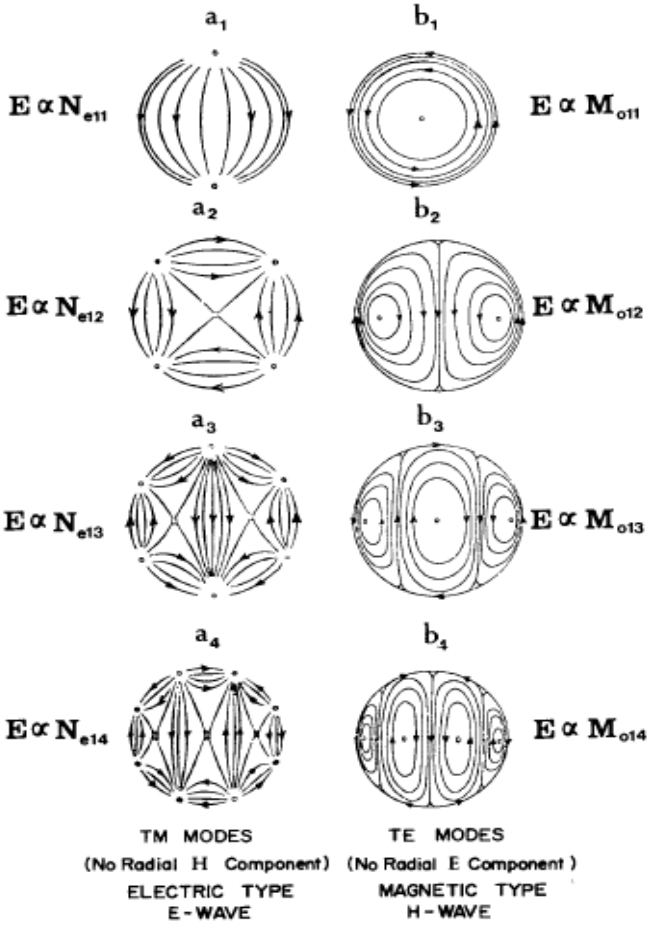

Figure 3.4. Normal modes according to the Mie theory. Picture taken from [3].

4 Photoluminescence

The previous chapters were dedicated to the introduction to plasmonics including localised surface plasmon polaritons. The subject of this chapter adresses the related main field of interest of this diploma thesis, i.e. photoluminescence.

Luminescene in general is surplus electromagnetic radiation emitted by material above the thermal radiation described by Planck's law. From the thermodynamical point of view it is a non-equilibrium radiation, therefore for its continuation it is neccesary to deliver energy. Luminescent phenomena are classified according to the method of energy supply into different types. If excitation energy is delivered via electromagnetic waves, the emission process is called photoluminescence. Other frequent types of luminescence are for instance electroluminescence, cathodoluminescence and chemiluminescence.

Photoluminescence (PL) differs from other types of secondary radiation (Rayleigh or Raman scattering or Cherenkov radiation) with its finite decay lifetime. This is because at photoluminescence the excitation energy is absorbed in the material and electrons are excited to higher energetic states and the reverse transition of electrons is followed by photon emission.

This chapter deals with photoluminescent properties of bulk and quantum dot semiconductors.

4.1 Excitation

As it was mentioned above, at PL electrons are excited to higher energetic states by absorption of the excitation energy. In case of semiconductors electrons are excited from the valence band to the conduction band. Therefore to understand a mechanism of photoluminescence it is important to investigate interband absroption properties of semiconductors.

It is apparent that electrons can be excited from a valence band to a conduction band only by absorbing a photon with higher energy than the energy band gap of the semiconductor ($\hbar\omega > E_g$). Also the electron transition has to be allowed in sense of selection rules and the Pauli exclusion principle must be also respected. The excited electron leaves an unoccupied state at the initial energy E_i, which is equivalent to the creation of a hole. Therefore, the interband absoprtion of the excitation energy can be considered as the creation of an electron-hole pair.

The bound electron-hole pairs (so called excitons) play also an important role in the light absorption and in luminescenct properties of semiconductors. However, stable

excitons do not exist in semiconductors at room temperature, only at very low temperatures [10], therefore their effect will be neglected in this study.

The interband absorption depends also strongly on the band structure of the semiconductor. In a direct gap semiconductor, where both the valence band maximum and the conduction band minimum, occurs at the center of the Brillouin zone (*k= 0*), electron can be excited simply by photon absorption. The transition is represented by a vertical arrow in the *E-k* plot (see Figure 4.1), because the photon momentum at optical frequencies is negligible compared to the typical momentum of excited electrons (wich is related to the size of the Brillouin zone). This means that the electron wave vector does not changes significantly by the transition. However, in an indirect gap semiconductor, where the conduction band minimum is usually at the edge of the zone (see Figure 4.1), the excitation is not possible only via photon absorption. Phonons must be involved to provide the significant change in the electrons wave vector.

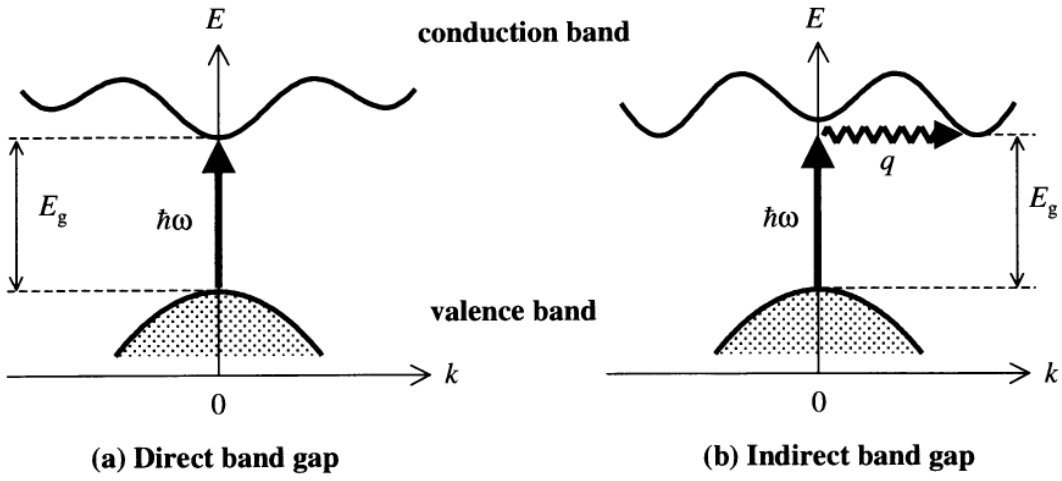

Figure 4.1. Electron excitation in a direct (a) and indirect (b) gap semiconductor. The vertical arrows represent electron excitation by photon and the wiggly arrow depicts impulse transfer by ponon. Picture taken from [11] pp. 51.

The transition rate is given in case of direct absorption by Fermi's golden rule:

$$W = \frac{2\pi}{\hbar}|M|^2 g(\hbar\omega) = \frac{2\pi}{\hbar}|\langle f|H'|i\rangle|^2 g(\hbar\omega), \qquad (4.1)$$

where g is the joint electron-hole density of states and M is the matrix element of the transition, which describes the effect of an external perturbation on the electrons. The symbol H' denotes the perturbation Hamiltonian, i and f characterises the wave function of the initial and final state, respectively.

In the electric dipole approximation the preturbation Hamiltonian equals $\boldsymbol{d}.\boldsymbol{E}$, where $\boldsymbol{d}$ is the electron dipole moment and $\boldsymbol{E}$ is the of electric field of the exciting radiation ([11] Appendix B). Therefore the transition rate can be written as:

$$I_0 = \frac{2\pi}{\hbar}|\langle f|\boldsymbol{d}.\boldsymbol{E}|i\rangle|^2 g(\hbar\omega). \quad (4.2)$$

The joint density of states in direct gap materials rises as $\sqrt{\hbar\omega - E_G}$ at photon energies higher than the band gap. In case of indirect gap materials the density of states depends quadratically on photon energy:$(\hbar\omega - E_G \pm \hbar\Omega)^2$, where $\hbar\Omega$ is the energy of phonons involved in the electron transition.

Considering the above mentioned dependences of the joint density of states, it is possible to deduce the frequency dependence of the absorption coefficient α (fraction of the absorbed intensity in a unit path length) from the absorption rate [11].

4.2 Emission

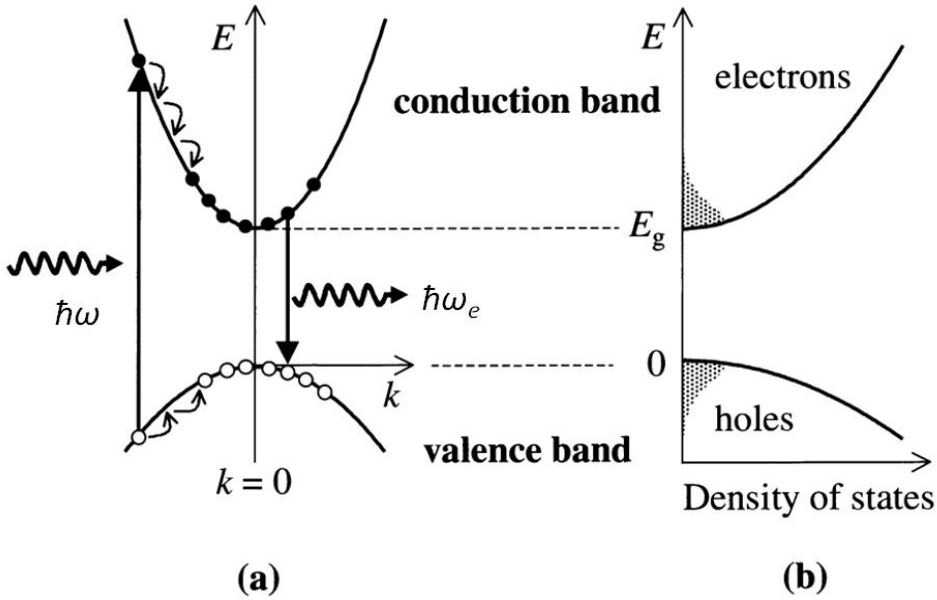

Figure 4.2. Picture a) shows a schematic diagram of the electron excitation, relaxation and photon emission. Density of states of electrons and holes is shown in the diagram b) including the thermal distribution (shaded) described by the Fermi-Dirac distribution. Picture taken from [11] pp. 98.

If the absorbed photons have the energy $\hbar\omega > E_g$ the excitated electrons have energy higher than the conduction band edge. However, after excitation electrons loose their energy within the conduction band very fast by emission of fonons (see figure 4.2 a). This series of events is known as electron relaxation and it occurs is due to strong electron-phonon coupling. Electron relaxation is much faster process (hundreds of femtoseconds) than the electron- hole recombination (nanosecond range), therefore electrons are able to relax to the bottom of the conduction band long before they are able

to emit a photon. The same relaxation process takes place in the valence band with holes. The distribution of electrons at the bottom of the conduction band is given by the Fermi-Dirac statistics (see Figure 4.2 b).

Following the electron (and hole) relaxation the recombination of electron-hole can occure. As in case of the absorption, the energy and momentum conservation laws must be fulfilled and the Pauli exclusion principle cannot be violated by the recombination. The intensity of photon emission (number of emitted photons from a unit volume in a unit time) is given by the following simple equation:

$$I = \frac{N}{\tau_R}, \tag{4.3}$$

where N is the instantaneous concentration of excited electrons in the conduction band and τ_R is the lifetime of the radiative of the transition. Equation (4.3) says that the number of emitted photons is proportional to the concentration of excited electrons and inversely proportional to the radiative lifetime. However, electron-hole recombinations can occur also non-radiatively without photon emission. Energy is released in this case in form of heat (phonons) or is discharged into defects and impurities. Ultimately the change in the concentration of excited electrons is given by three factros: radiative and non-radiative recombination and the excitation. The non-radiative recombination is characterized with its lifetime τ_{NR} like the radiative transition and the excitation is expressed with a quantity G, which is the number of excited electrons per unit volume and in unit time. Using a simple approximation the excitation can be expressed as the product of the absorption coefficient and the intensity of the excitation ligth I_0: $G = \alpha I_0$ ([10] page 113). The change in the concerntration of excited electrons can be written as:

$$\frac{dN}{dt} = G - \frac{N}{\tau_R} - \frac{N}{\tau_{NR}} = \alpha I_0 - \frac{N}{\tau_R} - \frac{N}{\tau_{NR}}. \tag{4.4}$$

It is apparent, that when the radiative lifetime is shorter than the non-radiative lifetime, the dominant channel of recombination is the photon emission.

From practiacal point of view two situations are important: stationary state when the intensity of luminescence is constant and the decay of the luminescence when the excitation is turned off (G=0). In this work only the stationary state will be investigated (time resolved measurements are not available).

The stationary state is characterized by the condition $dN/dt = 0$. Intensity of luminescence can be expressed by inserting this condition and equation (4.3) into (4.4):

$$I = \eta \alpha I_0, \tag{4.5}$$

where η denotes the qauntum efficiency (or quantum yield) of photoluminescence defined as:

$$\eta = \frac{\frac{1}{\tau_R}}{\frac{1}{\tau_R} + \frac{1}{\tau_{NR}}} = \frac{\gamma_R}{\gamma_R + \gamma_{NR}} = \frac{\gamma_R}{\gamma} \leq 1, \tag{4.6}$$

where γ_R and γ_{NR} is the radiative and non-radiative decay rate respectively defined as a reciprocal value to the corresponding lifetime. The sum of these decay rates gives the total decay rate γ. The value of quantum efficiency gives the ration between the probability of the radiative recombination and the probability of the total recombination. Typically the quantum yield of strongly pohotoluminescent materials is much less than 1, as a rule in the orders of 10^{-1}.

It is important to emphasize that the linear dependence of the luminescent intensity on the excitation intensity is generally valid only for ideally clean, intrinsic semiconductors. The impurities and dopants present in semiconductors create luminescent centers in the material which give arise to new radiative recombination channels, resulting in more complex intensity dependence. However, discussion of these luminescent centers is beyond the scope of this thesis.

4.3 Photoluminescence of semiconductor quantum dots

Low dimensional semiconductors have many new interesting optical properties compared to bulk materials. In the following a few basic features of the quantum dots will be qualitatively mentioned.

Quantum dots are low dimensional structures with a confined size in all three directions. The charactreristic dimesions of these nanostructures (often called also 0D structures) are in units of nanometers. At such a small size of structures their optical properties are different from the bulk properties. The deviation is due to the quantum confinement effect, which is significant when the size of the nanostructure is comparable with the de Broglie wavelength of electrons and holes in the material. The strong spatial confinement of electrons and holes in the quantum dots results in discrete energetic states, like in case of individual atoms. The position of energetic levels in the valence and conduction band can be tuned by size modification.

The next important property of quantum dots is that excitonic effects are observable in absorption and emission spectra even at room temperature [10]. Stable excitons at room tempereature are possible in quantum dots because electrons and holes are forced to be close together resulting in an enhanced Coulomb interaction between them.

As a result of quantum confinement, PL spectra of quantum dots are shifted to higher energies (blue shift) compared to the bulk material. Furthemore, the increased overlap of the electron and hole wave functions leads to the increased quantum yield.

Relaxation mechanisms are also very efficient, therefore mostly one emission peak is significant in the spectra which is attributed to the allowed transition at the lowest energy.

It is important to note, that from the technological point of view, it is impossible to manufacture quantum dots with exactly the same size. This finite size distribution results in broadening of the emission and absorption spectrum peaks.

4.4 Plasmon-enhanced photoluminescence

In his pioneering work in 1946 Edward Mills Purcell reported that the radiative emission rate is influenced by the environment in which the emitter is placed [1]. This effect (later named after Purcell) was later widely investigated in connection with surface enhanced Raman spectroscopy (SERS) [12]. The first modells describing the interaction of plasmons with photoluminescent materials were proposed alredy in the 1970s and 1980s [13,14], but the experimental work was lacking at that times. However, in the past few years many experimental works dealing with the plasmon-controlled luminescence were published due to appearance of new advanced nanofabrication and charcterisation techniques [15,16].

In general, there ar two ways how plasmon polaritons can affect the emission properties of photoluminescent materials:

- via local field enhancement
- via decay rate modifications.

Local field enhancement

It is known that under resonant conditions the electric near field around metallic particle can be enhanced by the orders of magnitude. If an emitter is placed in the vicinity of such a metallic particle, the emitter will be excited with the enhanced field, resulting in a strong enhancement in absorption and possibly emission related to the luminescent material (see equations 4.2 and 4.5).

To achieve enhancement in luminescence by local field enhancement it is important to match the LSP resonance frequency of the metallic particle with the excitation frequency. This is possible by appropriate choice of the size, shape and material of the metallic nanoparticle.

Decay rate modification

The physics behind plasmon induced decay rate modification is more complicated compared to the local field enhancement. It works in both ways: it can enhance but also strongly quenche the PL. The brief essence of this phenomena is that presence of metal nanoparticles or surfaces has a strong impact on the lifetime of PL. It occurs due to the energy transport between the metal and the emitter and due to LSP excitation. As a consequence, the quantum yield of the emitter is modified.

Decay rate modifications were first investigated using classical electrodynamic calculations for emitting molecules near metal surfaces [13, 17]. The first model describing the effect of small metal spheres on emitters decay rates was proposed by Gersten and Nitzan [12]. This model uses the quasi-static approximation for computing the electric field around the metal sphere, which gives inaccurate results for big spheres and vanishingly small emitter-sphere separations. The first exact calculation methods were proposed by R. Ruppin [14] and by T.F.George et al. [18] in the 1980s.

According to these models, emitters are represented as classical damped dipoles, where damping is characterised with a total decay rate (see equation (4.6)). The radiation from the emitter is scattered on the sphere and this scattered field at the dipole position acts as a driving force for dipole oscillations. This force is incorporated to the equation of motion of the dipole emitter and in the result it causes modification in the total decay rate.

The modification of the radiative decay rate is determined by comparing the energy fluxes through a surface of a very large imaginary sphere containing the metal sphere and without the sphere. Modification of the non-radiative decay rate can be than computed as a difference between the modified total decay rate and the radiative decay rate.

The modified (or apparent) quantum yield of the dipole emitter in the proximity of a metal sphere can be written as:

$$\eta_E = \frac{\gamma_R}{\gamma_R + \gamma_{NR} + \gamma_{NR0}} = \frac{\gamma_R}{\gamma}, \tag{4.7}$$

where γ_R and γ is the modified radiative and total decay rate, respectively, γ_{NR0} the non-radiative decay rate without the metal sphere and γ_{NR} is the non-radiative decay rate assiciated with the absorbtion in the metal sphere. The radiative and total decay rates can be expressed analytically for two main dipole orientations with respect to the metal sphere (radial and tangential) [18]. By a weighted average of the two basic orientations it is possible to compute also decay rates for orientation averaged over all solid angles [19]. For simplicity, the results will be introduced only for the radial dipole orientation ($\perp$):

$$\frac{\gamma^{\perp}}{\gamma_{R0}} = 1 + \frac{3}{2} Re \sum_{l=1}^{\infty} (2l+1) l(l+1) b_l \left[\frac{h_l^{(1)}(kr)}{kr} \right]^2 \tag{4.8}$$

$$\frac{\gamma_R^{\perp}}{\gamma_{R0}} = \frac{3}{2} \sum_{l=1}^{\infty} (2l+1) l(l+1) \left| \frac{j_l(kr) + b_l h_l^{(1)}(kr)}{kr} \right|^2, \tag{4.9}$$

where $\gamma^{\perp}$ is the total decay rate, $\gamma_R^{\perp}$ is the radiative decay rate in the radial dipole orientation, respectively, γ_{R0} is the radiative decay rate in the absence of the sphere, l is the angular mode number, r is the distance between the emitter and the sphere center, b_l

is the Mie scattering coefficient, $h_l^{(1)}$ and j_l are the ordinary Hankel and Bessel functions, respectively.

The results of this theory suggest that resonant coupling of the emission to the surface plasmon modes results in enhancement in both radiative and nonradiative decay rates. Depending which rate is dominant, the quantum yield can be signifacantly enhanced or decreased. Furthermore, the quantum yield enhancement is strongly dependent on the sphere size and the emitter-sphere separation.

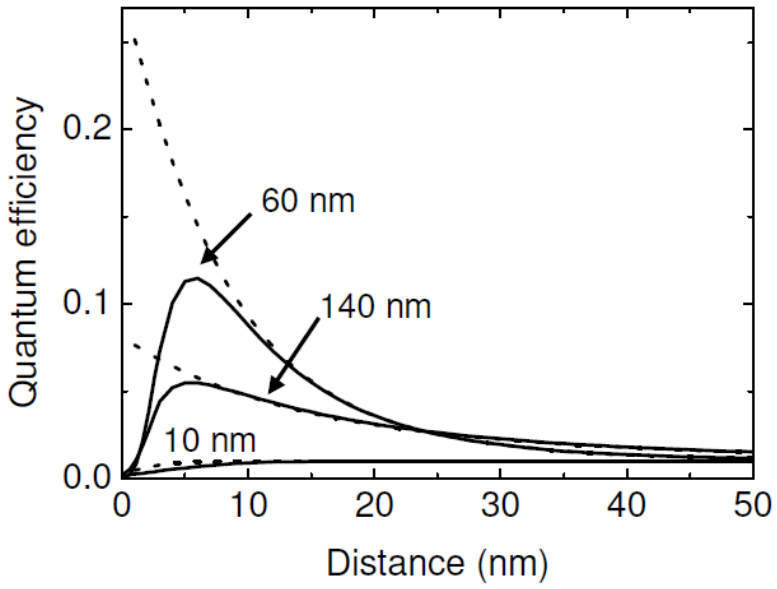

Figure 4.3. Quantum yield enhancement depending on the distance between the emitter and silver sphere for different sphere diameters (10 nm, 60 nm,140 nm) by taking into account coupling to all plasmon modes (solid lines) and by coupling to the dipole mode only (dashed lines). The quantum yield of the emitter in the absence of the sphere is 0.01. Picture taken from [19]

Figure 4.3 shows the quantum yield enhancement according to the exact electrodynamical calculation for emitter-sphere orientations averaged by all solid angles. The enhancements are calculated at emission wavelengths, where the radiative decay rate enhancement is maximal.

According to the calculations, there is an ideal emitter-sphere separation at which the efficiency enhancement is maximal. This can be attributed to the different distance dependence of the radiative and non-radiative decay rates. The enhancement of the non-radiative decay rate is much bigger at short distances (below 5 nm) than radiative decay rate enhancement. At these short distances the emitter excites higher plasmonic modes due to the strong field-gradient, even if they have different frequencies. Higher order plasmon modes are confined to the sphere surface, hence coupling to them increases the non-radiative decay rate frequency. It is also apparent from the dashed lines in the Figure 4.3, that if only coupling to the dipole mode is considered, the quantum yield increases

monotonously by decreasing the distance (it is possible to express the contribution of individual plasmon modes to the decay rate enhancement by considering only one non-zero Mie coefficient in the general realtionships (4.8)-(4.9)).

To explain dependence of the enhancement on the size of the metal sphere the so called radiating plasmon model [20] can be used. Although this only hypothesis it explains the experimental results very well. This model predicts the emission enhancement based on the optical properties of metal spheres using Mie- theory.

The ability of small spheres to absorb and scatter the incident light into the far field is characterized according to the Mie theory [3] by absorption (C_A) and scattering (C_S) cross sections. It is known, that at LSP resonance these cross sections can many times exceed the physical cross section of the sphere. For very small sphere diameters the absorption cross coefficient strongly dominates over the scattering cross section, which means the sphere absorbs very effectively the incident radiation. As a result, the luminescence is always quenched for small spheres (in case of silver it means less than 20 nm in diameter and for gold less than 40 nm). With an inceasing sphere diameter the scattering starts to dominate, which means the spehere scatters the incident light effectively to the far field. Effective scattering is than attributed to the enhancement of the PL. On the other hand for larger spheres the quantum yield decreases due to increased mode volume [21], which results in existence of an optimal sphere diameter. According to the exact calculation the optimal sphere size is 55 nm for silver and 110 nm for gold [19].

The dependence of the emission enhancement on the sphere's size can be alternatively explained in a slightly different way: to achieve emission enhancement is it important not only to provide resonant coupling of the emitter to the LSPs, but it is also important to achieve outcoupling of the LSPs into radiation. This outcoupling is negligible for very small spheres but for certain sphere diameters it can be very significant.

For computing the decay rate modification in the presence of metallic objects a free online available software can be applied [22]. This program enables us to compute decay rate and quantum yield modifications caused by spherical and ellipsoidal metallic particles using an exact electrodynamic method or an improved Gersten Nitzan model [19].

To summarize, the two mechanisms which give arise to the plasmon-enhanced photoluminescence were introduced above. It is important to note that these mechanisms are related to different frequencies: the local field enhancement to the absorption frequency and the decay rate modification to the emission frequency. Therefore, to achieve both enhancements, the nanoparticle should have LSP resonances at both frequencies.

Te overall intensity enhancement can be expressed as:

$$\frac{I_E}{I} = \frac{\eta_E(\omega_{EM})}{\eta} \frac{|\boldsymbol{d}.\boldsymbol{E_E}(\omega_{abs})|^2}{|\boldsymbol{d}.\boldsymbol{E}(\omega_{abs})|^2}, \tag{4.10}$$

where I_E , η_E and $\boldsymbol{E_E}$ is the enhanced PL intensity, quantum yield and electric field, respectively, and I, η and $\boldsymbol{E}$ are the initial values without the presence of the metal nanoparticles.

5 Apparatus for photoluminescence measurements

Our institute is not equipped with a commercial instrument for measuring photoluminescent spcetra, so there was a task to design and assemble an experimental set-up for that purpose. A tunable UV-laser and spectrophotometer were already available, but a proper sample holder and optical system to collect the photoluminescent signal was lacking. This chapter deals with describing the proposed apparatus and with its calibration.

Figure 5.1 shows the proposed set-up of the apparatus. The main parts are the excitation source (E), the sample holder (H), the collecting optics and the spectrophotometer (SD). The secondary branch with the light source (L) and CCD camera provides illumination and selection of the sample area to be investigated, and also helps to properly set positions of L1 and L2 lenses (imaging the sample plane to the entrance slit of the spectrophotometer).

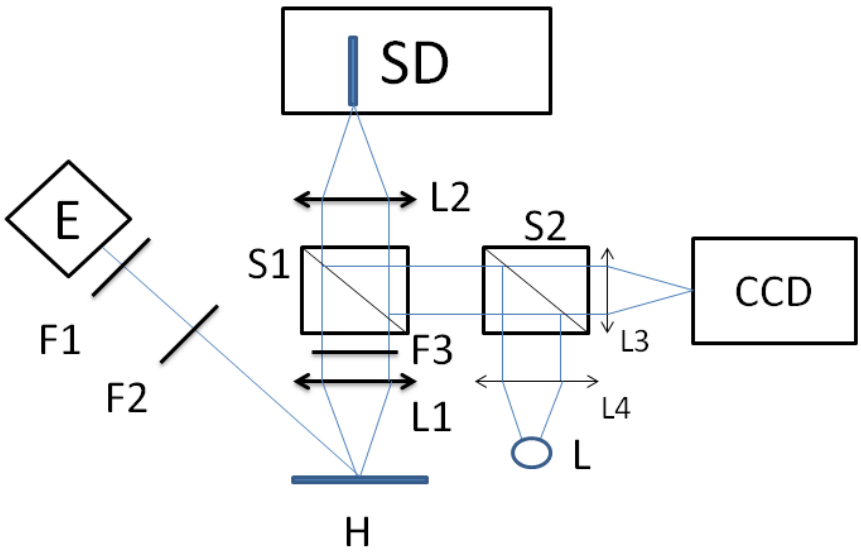

Figure 5.1. Schematic of the set-up for PL measurements. E- excitation source, H- sample holder, SD- spectrophotometer (spectrograph and detector), F1 to F3- filters, L1 and L2- focusing lenses, L3 and L4- auxiliary lenses, S1 and S2 beamsplitters, L- ligth source.

5.1 Components

Excitation source

The excitation source is a countinous, unpolarized He-Cd laser from CVI Melles Griot Co., with a tunable emission wavelength between 325 nm and 442 nm and a maximum emission power of 15 mW. The laser emitts ligth also at higher wavelengts, therefore filter (F1) is used to supress the radiation at higher wavelengths.

The filter F1 is a bandpass interference filter from Edmund Optics Inc., with a center wavelength of 326 nm and a 10 nm full width at half maximum. It also reduces the laser intensity at this wavelength by more than 70%.

The filter F2 is a variable neutral density filter, which enables to change continously the intensity of excitiation. The transmission of the filter can be adjusted from 100% down to 0.01% by its rotation.

Sample holders

There are two proposed sample holders to the apparatus. The first one is a small aluminium plate with a tantalum clip to fix the sample (see Figure 5.2 b). The aluminum plate is attached with a screwe to a 3-axis miniature translation stage. The stage is fixed to the table via magnetic base.

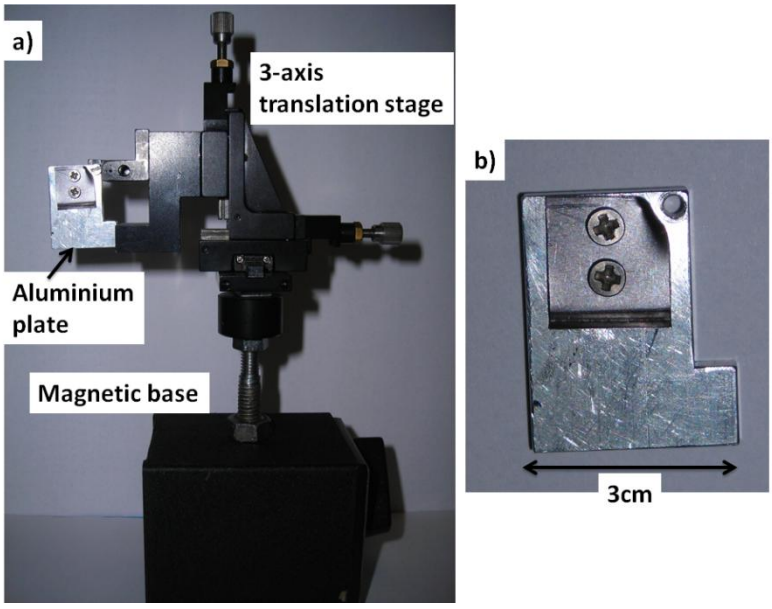

Figure 5.2 a) Image of the first sample holder. b) Detailed image of the aluminum plate on which the sample is mounted using a tantalum clip.

The advantage of this holder is that it enables quick sample mounting. On the other hand changing the sample requires removing the whole holder from the table by unbinding the magnet base. Therefore the position of the holder needs to be again set manually afterwards.

The apparatus will be also used for the measurements in transmission regime, therefore a second sample holder was designed. The holder is again fixed to a 3-axis translation stage but in this case for mounting and changing the sample the translation stage can stay fixed to the table and only the holder is removed from it. It significantly reduces the time required for refocusing the signal light after exchanging a sample. The sample holder is a 5cm x 15cm x 1cm aluminium plate being fixed to the translation stage with two bolts. Samples can be mounted to it from both sides over the hole drilled through the block. In the transmission regime the samples are mounted on the rear side with two tantalum clips. In the reflection arrangement a thin copper plate is placed over the hole on the front side of the aluminium block and the samples are fixed to this plate again with tantalum clips (see Figure 5.3b).

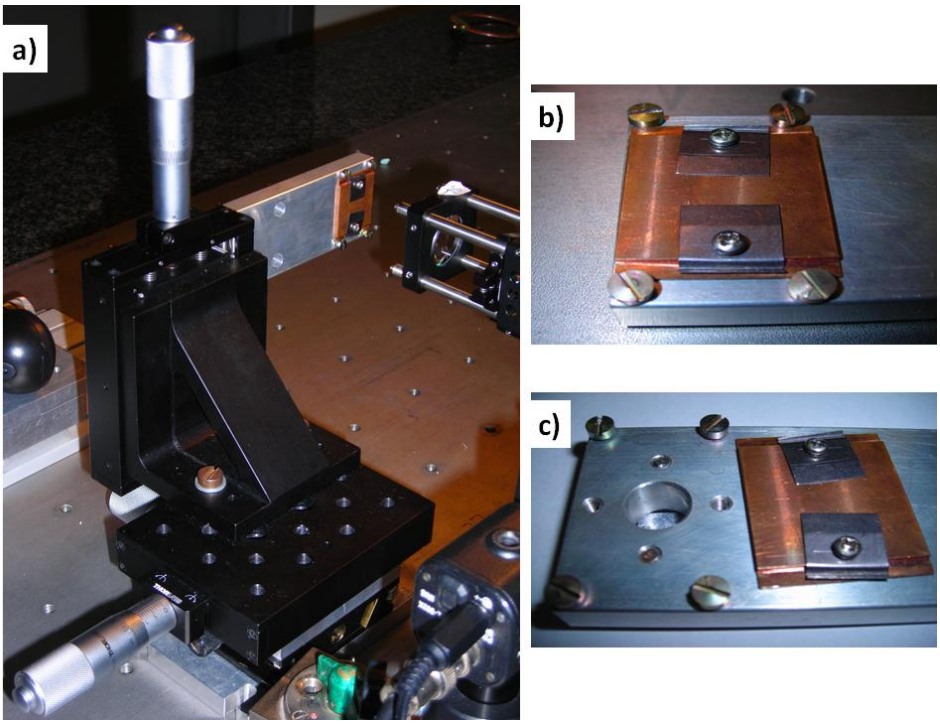

Figure 5.3. a) Image of the complete sample holder with the 3-axis translation stage. b) Detailed image of the front side of the sample holder with a fixed copper plate. The sample is fixed to the copper plate with tantalum clips. c) The front side of the holder with the uncovered hole for the transmission regime.

Further advantage of this holder is that due to wider tantalum clips and wider movement range in the plane of the sample it is possible to mount two samples in the holder at the same time. Also a much higher mechanical stability and the fine (micrometric) movement in the perpendicular direction to the sample plane is an advantage of the second sample holder.

The aluminium and copper plates were manufactured at the institute workshop.

Collecting optics

The main parts of the collecting optics are two focusing lenses. Both of them are made of fused silica to transmit UV radiation as well. This is neccesary, because some of the measured semiconductors (e.g. GaN, AlN) emit in the near UV region and classic lenses made of glass have a rapidly decreasing transmittance in that region.

As depicted in Figure 5.1, the sample is placed in the front focal plane of the first lense and the entrance slit of the spectrophotometer is in the back focal plane of the second lense. With this arrangement the emitted light is collected from a very small spot on the sample and subsequently focused on the entrance slit of the spectrograph. In this way the bunch of ligth between the lenses is paralell. The focal lengths of the first and second lense are 50mm and 100mm, respectively. The lenses were purchased from Thorlabs Inc. The focal length of the lense which focuses the light on the entrance slit was chosen to obtain a maximal brightness of the entrance slit of the spectrophotometer ([10] pp 76).

Usually, the scattered signal of the excitation laser is very strong compared to the PL signal, therefore a third filter (F3) was placed between the focusing lenses. It is a longpass filter which filters out wavelengths below 350 nm.

To provide correct focusing by the above mentioned lenses a secondary branch is available in the optical set-up. This branch contains a CCD camera and light source with lenses and two non-polarizing beamsplitter cubes (see Figure 5.1). According to the orientation of the first beamsplitter (S1) the ligth source illuminates either sample or the entrance slit. The focusing is done by adjusting the position of the lenses L1 and L2 to obtain a sharp image of the sample surface and the slit, respectively, by the CCD camera. Focusing on the slit has to be done just once and the lense L2 is fixed afterwards. However, focusing by the lense L1 has to be done after each sample exchange. During PL measurements the secondary branch is not used, therefore the beamsplitter in the primary branch (S1) can be easily removed.

It is possible to provide focusing by L1 even without external light source, if the sample possesses a strong PL in the visible region upon excitation. In this case the second beamsplitter (S2) can be also removed and the CCD camera captures the luminescent surface.

Spectrophotometer

The emitted light from the sample is detected with a pre-aligned spectrograph/detector system.

The signal is processed with a Shermrock 303i-A imaging spectrograph in a Czerny-Turner configuration with a focal length of 303 mm. It has a spetcral range from 190 nm to 10 μm and maximal resolution 0,1 nm. Three different diffraction gratings are built in it on a rotating turret enabling measurements for different resolutions and spectral ranges. A schematic view of the spectrograph is depicted in the Figure 5.4.

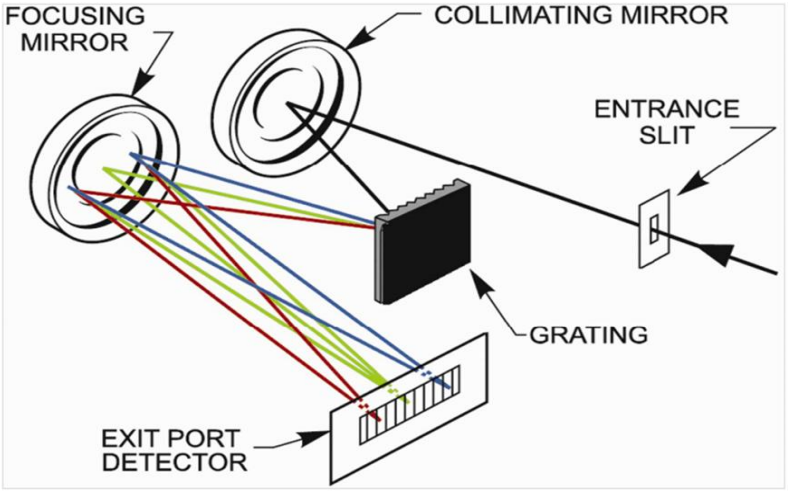

Figure 5.4. Schematic of the spectrograph (Shermrock 303i-A) in Czerny-Turner configuration. The picture was taken from the manual of the spectrograph.

The detector, which is an iDus CCD camera with a pre-amplifier and analog to digital converter, is attached to the spectrograph exit port (see Figure 5.4). The dispersed spectrum from the spectrograph is projected on a CCD camera chip, which has 1024 x 125 active pixels with a pixel size of 26 μm x 26 μm. During operation the CCD chip is cooled down thermoelectrically to -70˚C.

Both, the spectrograph and the detector were manufactured by Andor Technology plc. and are fully controlled by a computer. The accessories to the appratus, like cage plates, construction rods, post assemblies, different types of mounts and the translation stages were purchased from Thorlabs Inc. and partly available at our institute.

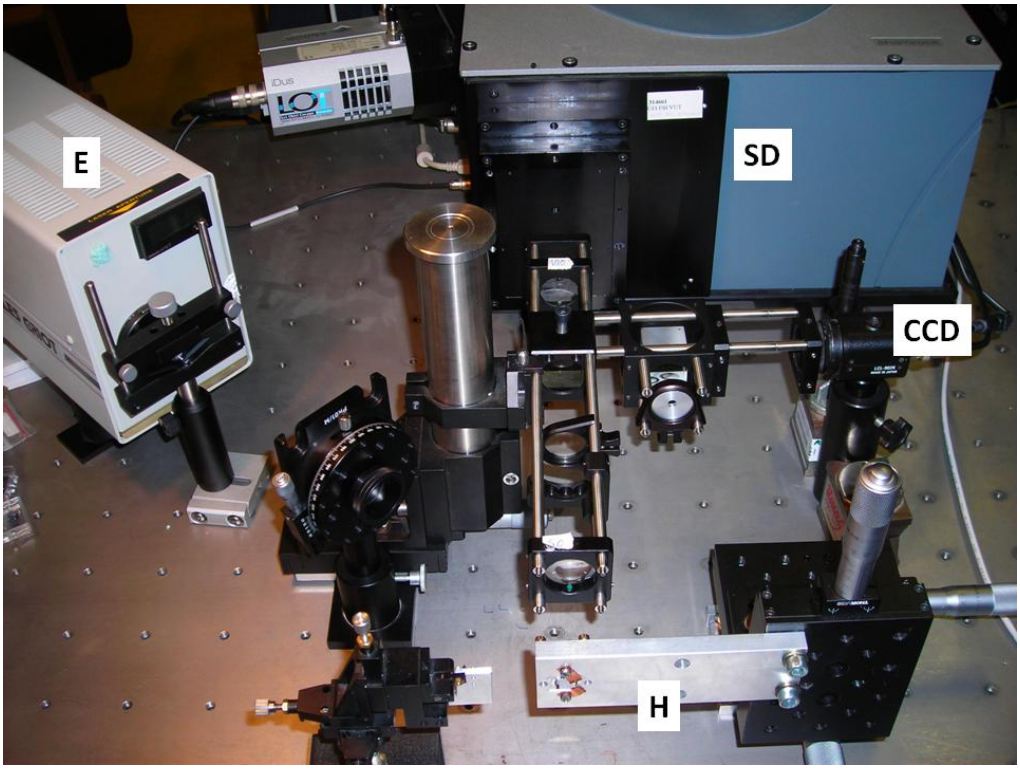

Figure 5.5. Image of the assembled apparatus. E- excitation source (He-Cd laser), H-sample holder, SD- spectrophotometer (spectroghraph/detector).

5.2 Calibration

Already the first tests with only surfaces and GaN samples showed that the spectrophotometer is not calibrated correctly. The scattered signal from the laser was detected by the spectrophotometer at λ = 312 nm instead of the correct value 325 nm. Therefore, the detector was calibrated using two lasers with defined emission wavelengths: the He-Cd laser and a green laser emitting ligth at 532 nm. The operating software enables a manual calibration of the detector using at least two defined wavelengths in the spectra (function "*Manual X-Calibration"*).

Instead of a sample a mirror was used to reflect the signal from the lasers to the detector In the acquired spectra the correct wavelength was assigned to the two measured sharp peaks. This calibration is very simple, but inaccurate as it uses only 2 points and a linear fit correspondingly.

Hence it is better to use a calibration file provided by the manufacturer. However, also this file does not guarantee the precise calibration. Due to the possible small changes in the grating turret position the spectra can be shifted from the real position, which has to be corrected using a well defined source and a function called "*Offset adjustment control*".

After the calibration the signal emitted from the laser was measured using a metallic mirror. Understandably the bandpass (F1) and the longpass (F3) filters were not used only the neutral density filter (F2) was kept in the branch to avoid saturation of the detector. Furthermore, the lenses showed weak PL upon direct laser radiation. Therefore the laser wasdirected to the detector without them, only using the mirror.

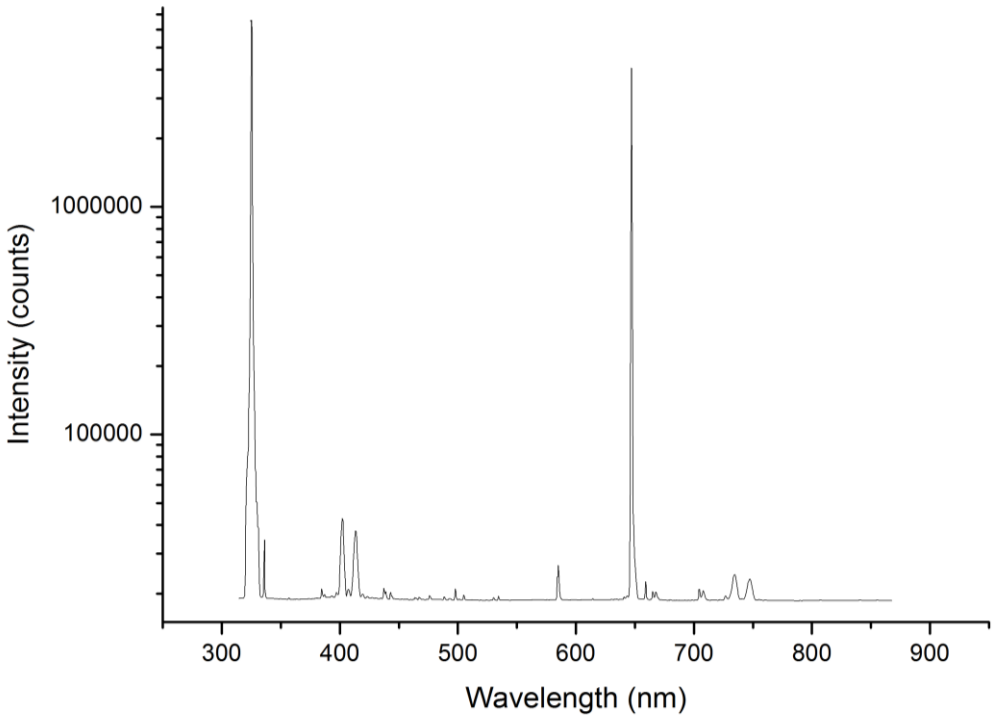

Figure 5.5. Emission spectrum of the He-Cd laser. The intensity is showed in logaritmic scale in order to visualise minor peaks as well.

It is apparent from Figure 5.5 that in addition to the main peak at 325 nm there is a sharp strong peak at 648 nm and few other less intensive peaks at differenet wavelengths. The peak at 648 nm was first considered as product of the laser second harmonics. However from the measured spectra it is apparent, that the peaks at 325 nm, 336 nm, 402 nm and 413 nm are repeated at higher wavelengths. These echoes are most likely caused by the spectrograph.

If the peak at 648 nm were generated by the laser, than using the bandpass filter F1 it should dissapear from the spectrum. Nevertheless this peak kept the same relative intensity with respect to the peak at 325 nm even after using such a filter. Similarly, the peaks at 402 nm and 413 nm are still present in the spectra. On the other hand, using the longpass filter F3 the peak at 325 nm should be less intensive than the peak at 647 nm, but again in the measured spectra they appear with roughly the same relative intensity. These results suggest, that the peaks at 402 nm, 413 nm and 648 nm do not originate from the laser, but they are caused by additional effects in the spectrograph.

To summarize the designed experimental set-up for the measurement of PL was assembled and tested. The measurements performed using this apparatus will be discussed in the next chapter.

Given that the apparatus is at its current place just temporarily, few operations like the proper fixing of the laser and the spectrograph have not been completed yet. The measurement of the laser emission spectra suggests that spectrograph should be improved in the near future. After getting more experience in adjustement and measurement with the apparatus, further modification should be considered after the transportation of the apparatus to its final location.

This modification refers to the excitation. In the current state the laser has a fixed position and the excitation beam aims directly from the laser at the sample. As the signal has to be collected from the spot where the sample is excited, this spot must lie on the optical axis, it means the sample cannot be moved along this axis. Therefore focusing to the sample plane should be done by moving the lense L1.

However, it would be more useful to direct the laser beam on the sample with a mirror or to excite with the beam perpendicular to the surface using a dichroic mirror (see Figure 5.6). In this arrangement the focusing is done only by moving the sample and the lense L1 can be fixed. Further advantage of this perpendicular arrangement is that it enables more localised surface excitation. In addition with a dichroic mirror the excitation could be filtered out from the measured spectra much more effectively (filter F3 is not of a good quality).

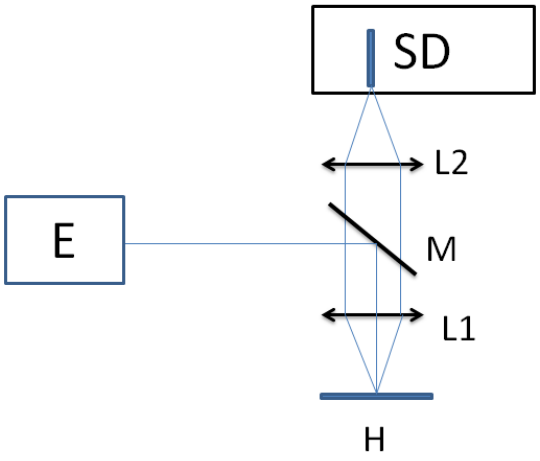

Figure 5.6. Recommended modification of the excitation arrangement. E-excitation source, H- sample holder, L1 and L2- focusing lenses, SD- spectrophotometer, M- dichroic mirror.

6 Measurements

This chapter contains the results of measurements performed on different planar samples and colloidal solutions of semiconductor quantum dots. The only bulk material from the measured samples was GaN, the others were low dimensional structures like nanocrystalline Si (ncSi) and CdTe quantum dots.

6.1 Bulk GaN and nanocrystalline Si

PL properties of these two samples are well know, thus they are suitable for testing the functionality of the apparatus.

The GaN sample was made using metalorganic chemical vapour deposition (MO CVD). The n-doped GaN thin film was deposited on a polished sapphire (0001) substrate and its thickness was 20 μm.

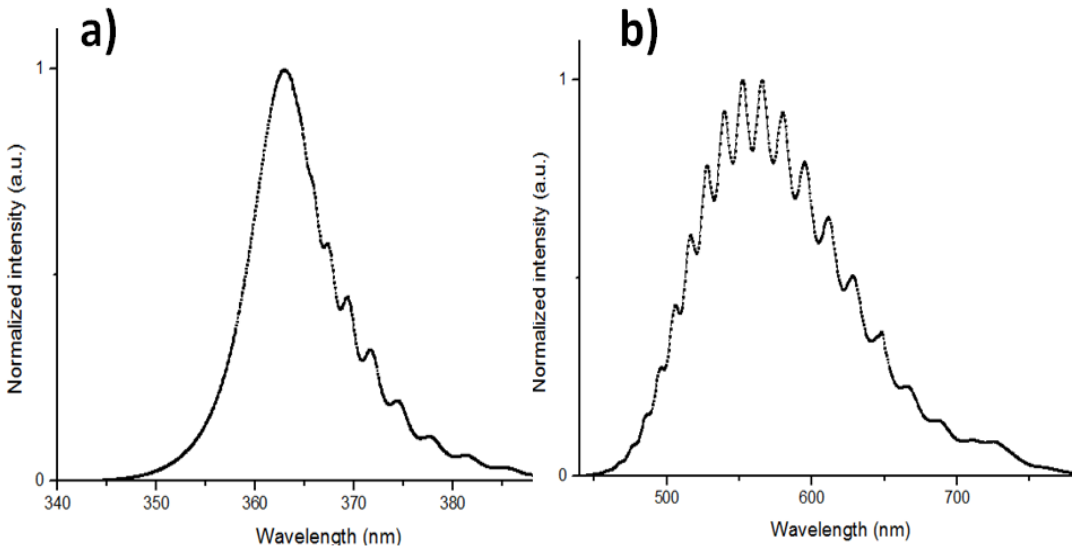

Figure 6.1. PL spectrum of epitaxial GaN on a sapphire substrate, excitation wavelength 325 nm. The PL peak in a) is attributed to the near -band gap transition and the peak b) is to Ga vacancies.

The GaN sample was excited at room temperature by He-Cd laser at 325 nm. As it is shown in the figure 6.1 GaN shows a strong PL peak at 362 nm and weaker broad PL

peak around 550 nm. The peak at 362 nm is attributed to 3.4 the eV band gap width of the GaN and the PL peak at 550 nm to the Ga vacancies [23]. Interestingly, PL intensity is modulated but only for photon energies lower than the band-gap width. This intensity modulation is due to the optical microcavity effect caused by the air/GaN and GaN/sapphire interface. For energies higher than the band gap the absorption in GaN supresses the modulation of the PL intensity [24], therefore the intensity is not modulated for wavelengths shorter than 360 nm.

The nanocrystalline Si (ncSi) powder was only recently obtained from the Institute of Physics, Czech Academy of Sciences in Prague and therefore it was measured only in powder form in plastic cuvette. The ncSi powder was produced by electrochemical etching of the p-type Si (100) and the size of its nanocrystals was between 3 and 4 nm [25].

The PL spectra of this material show a single broad emission peak around 635 nm (see Figure 6.2), which originates from the quantum confinement effect and a surface recombination channel [26].

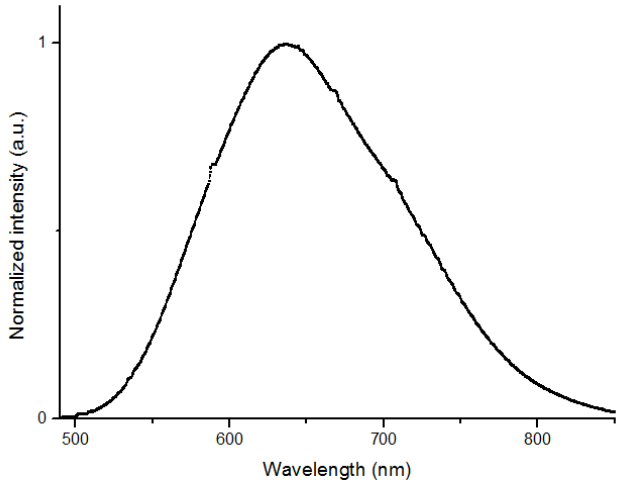

Figure 6.2. PL spectra of the ncSi powder excited by a He-Cd laser at 325 nm.

One can say that both the measured spectra of the GaN sample and the ncSi powder show a very good agreement with literature and data provided by the producers.

6.2 CdTe quantum dots

CdTe QDs were manufactured at the Institute of Analytical Chemistry the Czech Academy of Sciences in Brno. The QDs were available in form of colloidal solutions. Each of the four water solutions had a different pH value and consisted of QDs of different sizes. The QDs were dispersed in water using a stablizing agent to avoid their agglomeration. The stablizing agents in solutions with pH 4 and pH 6 are amino groups on the surface of the nanocrystals. In solutions with pH 7 and ph 11 the stabilizing agents

are carboxyl groups. The amino groups carry a negative charge and the carboxyl groups a positive one. These charges on the surface of the QDs prevent them from aggregation.

The quantum yield and the size of the QDs is not precisely known, but according to the producer, size of the QDs varies between 2 and 5 nm.

The QDs were first measured in the colloidal form in transparent jars. The jars were placed in a proper sample position using post holders. The measurement didn't require precise adjustement of the position due to the strong photoluminescence of the solution. The measured spectra are shown in the Figure 6.3.

It can be seen in the measured spectra that the size of the QDs significantly influences the emission wavelength because the emmission wavelength, it varies from 500 nm to 800 nm. The QDs show purely excitonic luminescence with a narrow emission peak as predicted in Chapter 4.3, with the emission maxima at 550 nm, 540 nm, 595 nm and 740 nm. The solution with pH 11 has a broader emission peak compared to the other solutions, which suggests wider size distribution of QDs. This curve is not symmetric because a shoulder is appering at shorter wavelengths, which suggests the presence of a second less significant peak at this peaks side. This feature will be discussed later in this chapter.

It is important to note that QDs show significant blue-shift in photoluminescence with aging. Measurements were performed also two months earlier and measured emission wavelengths were higher by 20 to 40 nm. This blue shift in the emission wavelength is well known and it is caused by photooxidation [27]. If the solution is under air and is exposed to ligth, the surface oxidizes, resulting in reduction of the QDs size and blue-shift in emission. The oxid layer on the surface of the QDs results in furthermore quenching of the photoluminescence [28].

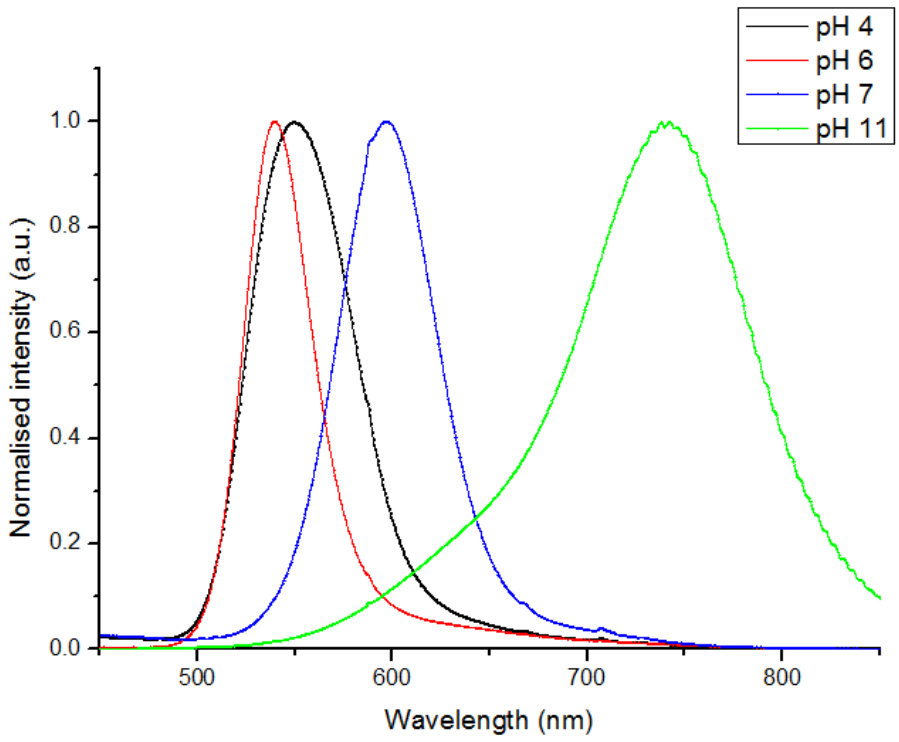

Figure 6.3. PL spectra of the CdTe solutions, excitation with the He-Cd laser at 325 nm. Emission maximum of the solution pH 4 is at 550 nm (black curve), for pH 6 at 540 nm (red curve), for pH 7 at 595nm (blue curve) and for pH 11 at 740 nm (green curve).

Unfortunately, the solution with pH 7 showed the visible signs of aggregation (also caused by photo-oxidation), therefore it was not used in the further experiments.

The next step was a deposition of the QDs on a substrate and subsequent measurement of PL from planar samples. The deposition was performed similarly as in case of gold colloid deposition on a Si substrate [29].

As a substrate, Si(100) was used with a resistivity of 6-9 Ωcm. The substrate was dipped into the solution for 1 hour and subsequently dried out by blowing with nitrogen. It is important to note, that the distribution of QDs is usually not even on the substrate. Ideally, the QDs are randomly distributed on the surface, as it is shown in Figure 6.4 a), but due to blowing with nitrogen the amount of deposited QDs can be very varied (see Figure 6.4b).

This sample preparation rudimentary, however it is sufficient for measuring the photoluminescence spectra.

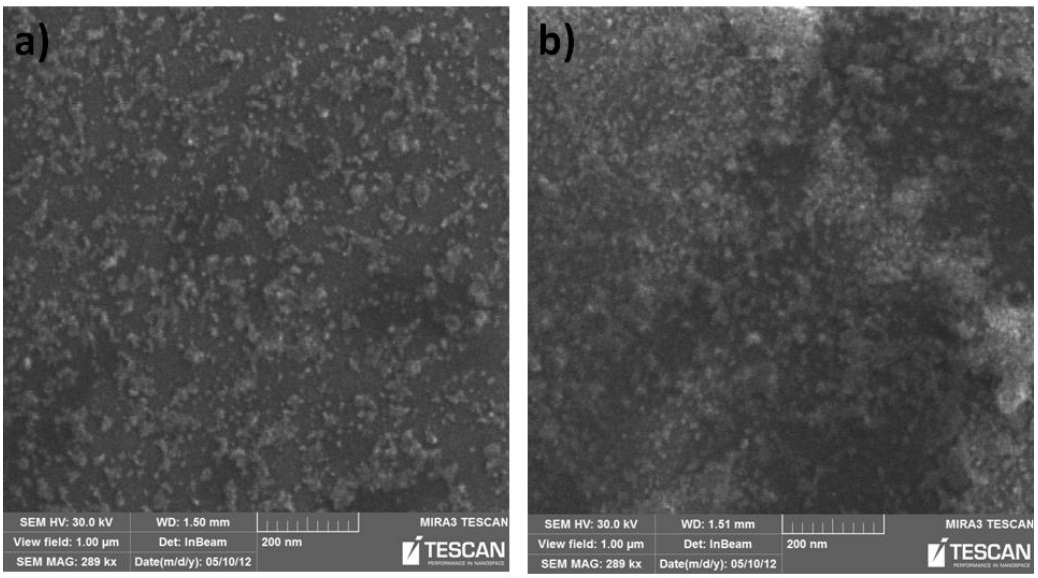

Figure 6.4. SEM images of the Si (100) surface after dipping the sample into solution of CdTe with pH 11 for 1 hour and blow-drying with N_2. Image a) shows the ideal random distributin of the QDs, where QDs appear as brighter features on the darker substrate's surface. Image b) shows the uneven distribution of the QDs caused by the blowing with N_2 on the same sample. Images were taken at Tescan.

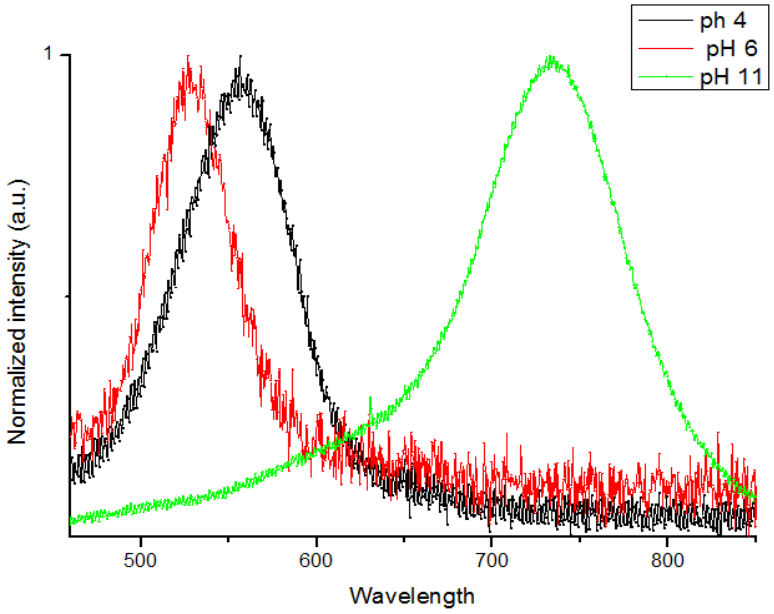

Figure 6.4. PL spectra of the CdTe quantum dots deposited on Si (100) substrate. Emission maxima are at 525 nm, 540 nm and 730 nm and the excitation wavelength is 325 nm.

As it is shown in the Figure 6.5, the emission wavelengths are further blue-shifted and the measured signals are much lower compared to the measurements in colloidal form, which is also attributable to the photo-oxidation of the sample's surface.

In order to obtain more homogenous and thicker layers of QDs on the substrate surface, spin coating method was used instead of dipping the substrate into the solution. 20 µl of the solution was placed on the substrate and then it was spinned for 1 minute at different rotation speeds (2000 rpm - 4000 rpm).

The PL spectra of the samples are identical for both preparation methods with one exception. Preparing the sample using spin coating from the solution with pH 11, the measured photoluminescence spectra in the centre and periphery of the sample are different. The measured spectra in the periphery are the same as in case of dipping the substrate into the solution (see Figure 6.4, black curve). However in the central part of the sample two peaks with the same intensity at 600 nm and 740 nm are visible in the spectrum (Figure 6.4. red curve).

These results suggest, that the CdTe particles of two different sizes are present in the solution with pH 11. Peak at 600 nm is attributable to a small amount of the particles of a smaller size compared to that one of the major particles, which give rise to the pak at 740 nm. Due to the rotation of the sample the bigger QDs tend to spin off from the central part more intensively than the smaller ones, leading thus changes in the ratio corresponding peak intensities.

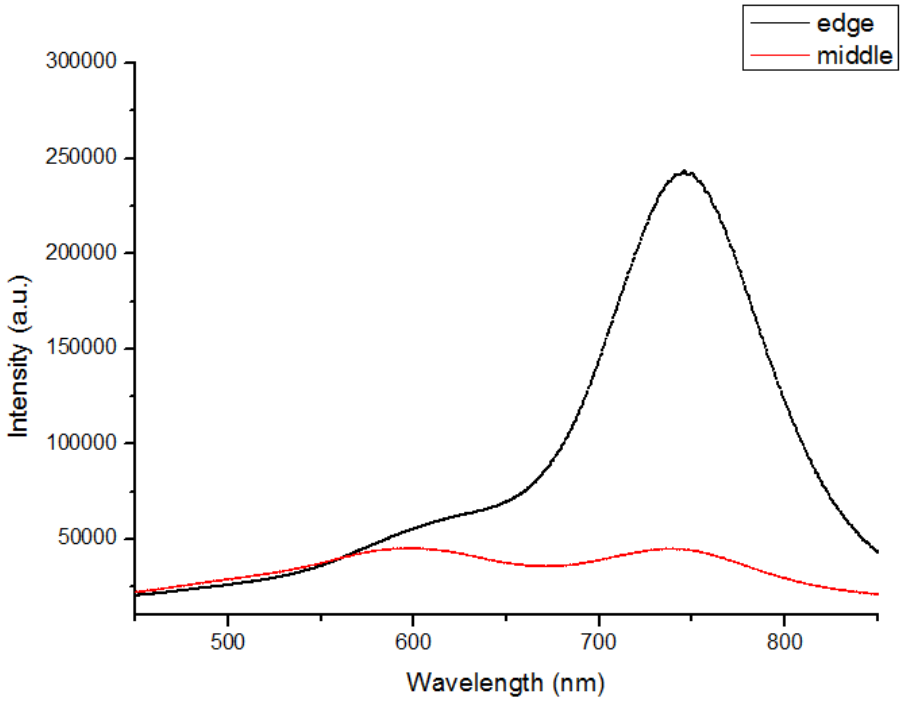

Figure 6.5. PL spectra of the sample prepared by spin coating using the solution with pH 11 on a Si substrate for 1 minute at a rotation speed of 2000 rpm. The red curve shows the PL spectrum in the middle and the black curve at the periphery of the sample. In the middle of the sample two peaks at 600 nm and 700 nm are distinguishable.

According to that, the previously mentioned shoulder in the PL spectra of the solution with pH 11 originates from contribution of smaller QDs present in the solution to the peak.

6.3 CdTe quantum dots and gold nanoparticles

In the previous chapter the preparation method of the planar samples consisting of CdTe QDs was discussed. This chapter deals with the fabrication of samples consisting both of metal nanoparticles and photoluminescent QDs. They could allow an experimental study of plasmon-enhanced PL.

As it was discussed in Chapter 4.4, plasmon-enhanced PL is a comlex phenomenon and parameters like the emitter- metal distance, metal nanoparticle size and material must be set correctly to provide enhancement. In order to choose these parameters correctly it is essential to exploit in the design of the samples simlulation and computational softwares.

The ideal emitter-metal distance can be calculated using the online software created by Polman et al. [22]. This software also enables us to calculate the enhancement of the quantum yield as a function of excitation light wavelength for spheres of different sizes and materials (see Figure 7.1). The only drawback of this software is that it enables to apply only homogeneous sphere surrounding medium, so possible effects of the substrate on the LSP resonances cannot be involved in the simulations.

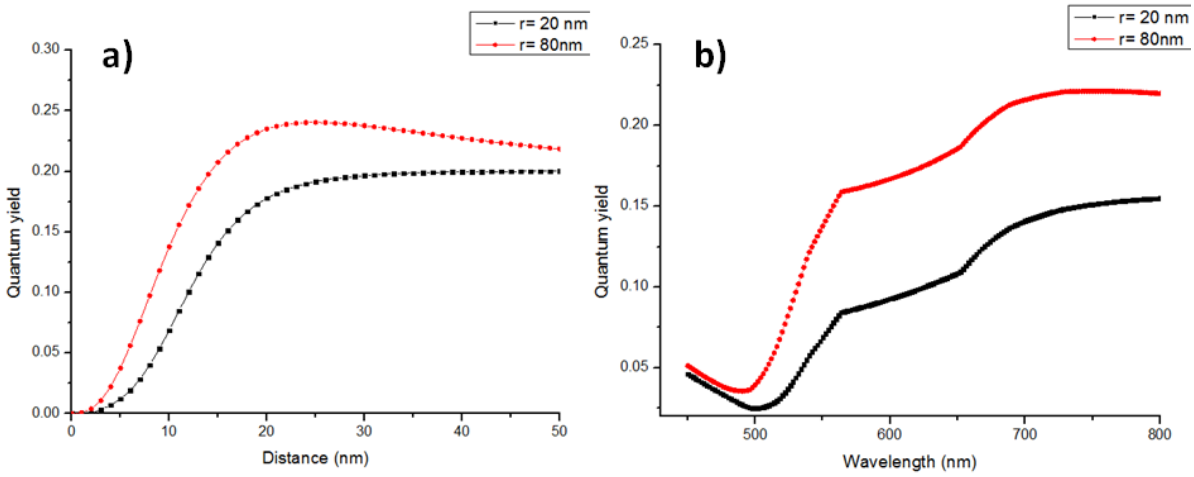

Figure 7.1. a) Dependence of the emitter quantum yield on the emitter-metal sphere distance in vacuum at emission wavelength of 550 nm. b) Dependence of the emitter quantum yield on the emission wavelength at fixed emitter-metal distance (10 nm). The reference quantum yield of the emitter is 0.2 and the size of the gold sphere is 20 nm (black curve) and 80 nm (red curve). Data were calculated using [22].

If the PL is enhanced by local the field effectt, the LSP resonance of the sphere has to match the excitation wavelength. The resonance wavelength of the nanospheres can be

computed using the Mie theory, but only in homogeneous media. Again, in case of the planar samples the effect of the substrate has to be considered, therefore instead of analytical calculations numerical simulations are recommended for computation.

The most commonly used numerical methods are the FDTD (Finite-difference time domain) and the FEM (finite element method). In one of the previous works at our institute the simulation of resonance wavelength of gold spheres on a Si substrate was done. The results showed that for a sphere diameter of 40 nm the LSPR resonance wavelength of the sphere on the surface of a Si substrate was red-shifted by 15 nm with respect to the sphere resonance in vacuum (see Figure 7.2). The simulations were made by the FDTD simulation software Lumerical.

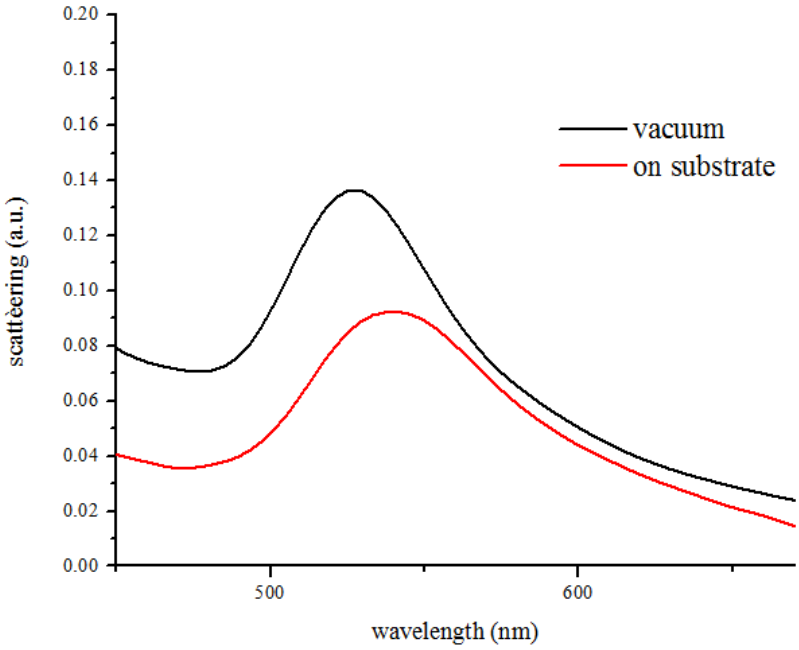

Figure 7.2. FDTD simulation of scattering of a gold sphere (r= 40 nm) into the far field as a function of the wavelength in vacuum (black curve) and for a Si substrate (red curve). Resonance of the scattering for the sphere in vacuum is at 527 nm and in case of the substrate at 542 nm.

Finally, once designing of samples the measurement method has to be considered as well. In case of measurements with high spatial resolution it is possible to detect PL from an individual QD, but the diffraction limit has to be taken into account. It means if we want to measure the enhanced PL of the single QD in the proximity of a metal nanoparticle, than in the minimal spatially resolvable region (which is typically around 1μm in diameter) cannot be other emitting QDs. Otherwise, the measured signal is the sum of emitted signals from all QDs inside the diffraction spot, which can give false results about the PL enhancement (for instance: the PL from some of the QDs is quenched and from others it is enhanced due to the distance dependence giving the same result as if there was no metal particle).

Using the assembled apparatus, discussed in Chapter 5, it is impossible to measure spatially resolved PL of the samples. The PL signal is integrated from the focused spot ($d \approx 10^{-1} mm$) on the sample. This requires the samples with homogeneous emission properties over the whole surface area.

Sample preparation

The samples were prepared using two solutions of CdTe colloids (pH 4 and pH11) and gold and silver nanoparticles in aqaeus solutions (purchased from BBInternational) on the Si (100) substrate. The metal particles are stabilized in the solution with citrate ionts on their surfaces resulting in a negative charge of the particles. Given that the QDs are also charged, a metal-QD interaction (and thus also separation) separation could be managed by an electrostatic interaction. Without this interaction the distribution of the QDs and nanoparticles should be stochastic.

The deposition of the QDs and metal particles was performed by dipping the substrate into the two corresponding solutions one after another.

Firstly, the gold particles were deposited on the Si(100) substrate by dipping the substrates into the solution of gold particles for 2 hours. Before deposition the pH of the gold solution was adjusted to pH 3.5 by adding HF acid to obtain a uniform coverage of the surface as it was discussed in [29]. The gold particles of a diameter of 20 nm were chosen since the depostion process for this particle size is well known from the previous experiments. The CdTe QDs were deposited also using the dipping methods for solutions with the pH 4 and pH 11 in the same way as it was discussed in the previous chapter.

Since the gold nanoparticles carry a negative charge and the QDs in the solution with pH 4 a positive charge, accumulation of the QDs at the gold spheres is expected resulting in quenching of PL. Furthermore, the estimated LSP resonance of the gold particles (530 nm) is close to the emission wavelength of the QDs (below 550 nm). Since the small gold particles tend to absorb the light at the LSP resonance rather than to scatter (see Chapter 4.4), further quenching of the PL is expected even for higher distances.

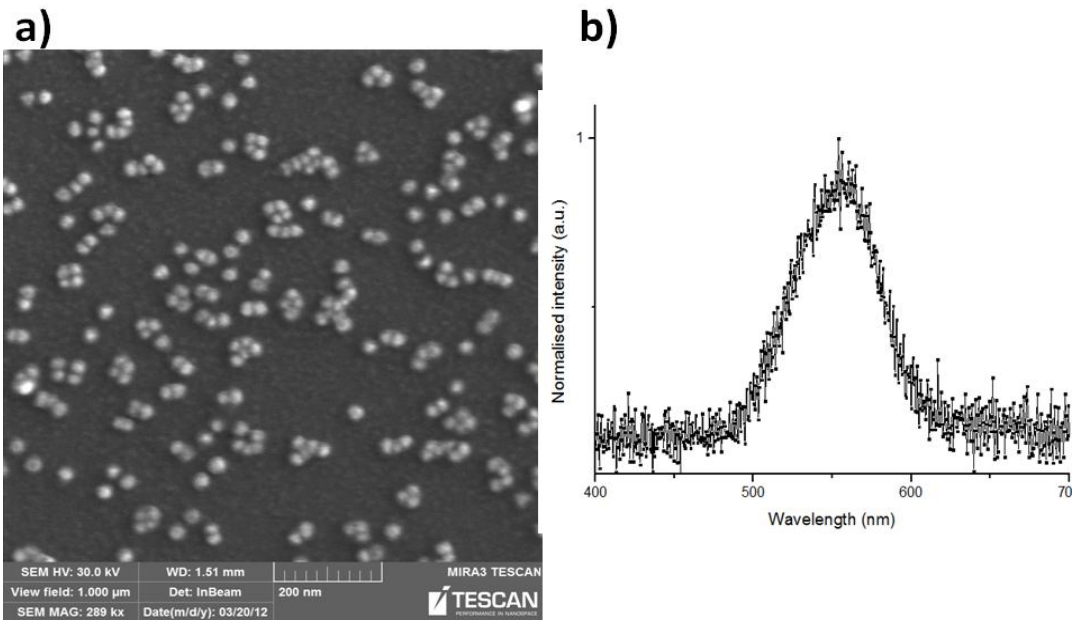

Figure 7.2. a) SEM image of the Si surface after deposition of gold nanospheres (d=20 nm) and CdTe QDs from the solution with pH 4. Bright dots are the gold nanospheres and the darker features between the spheres are the QDs. b) a PL spectrum from the prepared sample after excitation at 325 nm, with maximal intensity at 550 nm.

Figure 7.2 shows the SEM image of the surface with deposited golden nanoparticles and CdTe quantum dots (QDs solution with pH 4). The gold nanoparticles are clearly visible at the surface (brigth dots), but the QDs appearing as small darker spots between the gold particles are hardly distinguishable. From the SEM images it is not possible to say if the QDs are also on top of the gold particles. The measured PL spectra show a weak PL signal suggesting that QDs are present at the surface.

To evaluate the possible quenching, it is neccesary to prepare the sample without gold particles, but with the same QD concentration. However, it is hard to achieve since QDs tends to stick to the clean surface differently than to the gold deposited surface (in the mixed samples gold is deposited first and the QDs afterwards).

Therefore, an opposite order of deposition would be more suitable. However, by depositiong in the opposite order, the gold particles start to form clusters (very quickly after dipping), leading to deterioration of the solution. Furthermore, the QDs are detached from the surface, thus the opposite order of deposition is not feasible for sample preparation. Such a behavior is the same for the QDs solutions with both pH 4 and pH 11.

The second fabricated sample obtained gold nanoparticles (*d= 20 nm*) and QDs (deposited from the solution with pH 11) with an emission maxima at 730 nm. Since these QDs and gold particles carry negative charges on their surface, the certain separation between them on the substrate was expected. With an estimated LSP resonance for gold nanospheres at 525 nm the sample could be used for observing a PL enhancement by local field increase by excitation with a green laser at 532 nm.

Unfortunately, the SEM images showed an opposite effect of what was expected in connection with the electrostatic interaction between the QDs and gold particles. According to the Figure 7.3 the QDs are preferentially deposited around the gold particles and just a small amount of the QDs is on the substrate between the spheres. This behaviour can be partly explained by loss of the negative charge of the gold particles at the surface, but the correct explanation of this behaviour has not been explained yet.

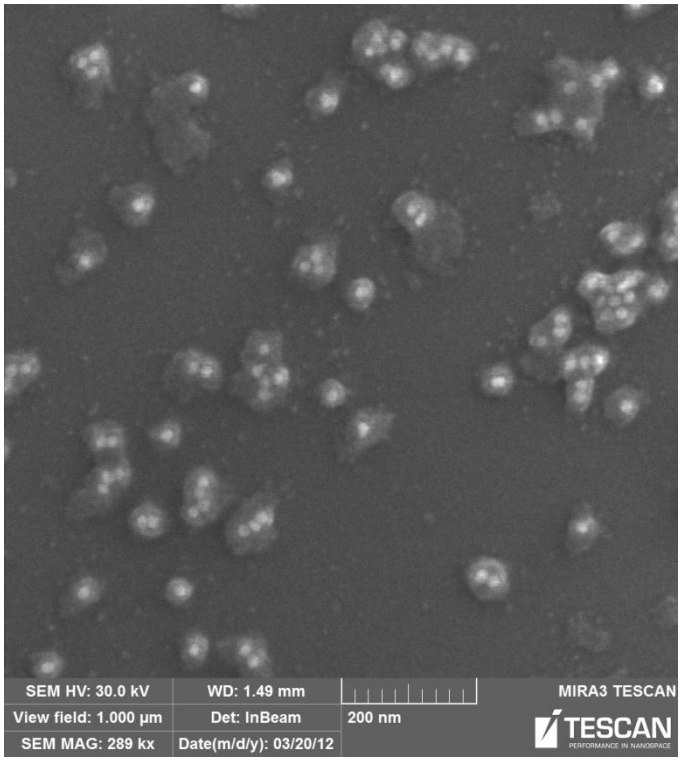

Figure 7.3. SEM image of the sample with gold nanospheres (*d= 20 nm*) and QDs (deposited from a solution with pH 11).

According to the Figure 7.3 again quenching of the PL is expected for the QDs near to the gold spheres. Furthermore, the LSP resonance of the gold spheres is certainly red-shifted due to the CdTe shell around the spheres therefore this sample is not suitable for the measurement of plasmon-enhanced PL in the predicted manner.

It is important to note, that by the deposition of QDs on the substrate covered with gold spheres a certain amount of the gold spheres detaches from the substrate. This effect is very significant for the solution with pH 11 (the concentration of deposited gold nanoparticles is reduced by more than 50%).

Conclusion

Two samples were fabricated by deposition of gold spheres and CdTe QDs on Si(100) substrates. Both orders of deposition were examined, but only successful deposition of both materials was found for metal-QD order.

The first sample was designed to demonstrate a quenching effect of PL. However, to confirm the quenching of PL on the manufactured sample, it is neccesary to have a reference sample possessing only QDs with the same concentration as in case of the mixed sample. To fabricate the reference sample it is neccesary to monitor the QD concentration on the surface, which requires more advanced measurement techniques due to the extremely small QD size.

The second sample was designed to observe the PL enhancement caused by local field enhancement at the excitation wavelength, but interestingly, instead of the the predicted repulsion, the attraction was observable between the QDs and gold spheres. The possible solution to this problem would be the application of QDs with a capping layer on their surface. The capping layer can secure a neccesary distance to avoid PL quenching at short distances.

Plasmon-enhanced PL will be investigated in the near future also for Si nanocrystals produced by high temperature annealing of silicon-rich oxinitride (SRON-SiO_xN_y) deposited using plasma enhanced chemical vapour deposition (PE CVD). The produced Si nanocrystals, embedded in silicon oxide or nitride, have PL in the near IR region (≈ 800 nm). In our institute it is possible to fabricate rectangular or cylindrical metal antennas by e-beam lithography or focused ion beam (FIB), which have LSP resonances in near IR region. The goal is to deposit SRON just in the gap between the metal antennas (e.g. by e-beam lithography) and to achieve a PL enhancement via the decay rate modification. The investigation and the sample preparation is in the early stage, therefore it will not be discussed here in more detail.

Summary

The diploma thesis dealt with a phenomenon known as plasmon-enhanced photoluminescence.

The principles of localised surface plasmon resonances and the photoluminescence are discussed in the theoretical part of the thesis. Furthermore the part contains the description of coupling between localised plasmons and photoluminescence.

The enhancement of photoluminescence by localised plasmons is achievable in two different ways: via field enhancement and through decay rate modifications. By the field enhancement the resonance of the localised plasmons enhances the exciting electromagnetic field, therefore it refers to the excitation of the photoluminescence. By decay rate modifications the localised plasmons resonances give rise to a new channel of radiative recombination, therefore it refers to the emission process in the pohotoluminescence. To achieve both enhancements the metal nanoparticles are required to support plasmon resonance at both excitation and emission wavelengths.

In the experimental part of the thesis an apparatus for measuring PL spectra in the visible region was designed and assembled. The apparatus uses a He-Cd laser for the excitation and the PL signal is transmitted to a spectrograph/detector by a set of lenses. The funcionality of the equipment was tested by measuring the PL spectra of GaN epitaxial thin film and nanocrystalline Si powder. The measurements were in a good agreement with the theory and previous studies of the given samples.

Furthermore, the PL spectra of four different solutions of colloidal CdTe quantum dots were measured. The measured emission spectra showed significant blue-shifts (up to 40 nm) with aging caused by photo-oxidation. The CdTe quantum dots were deposited on Si(100) substrates using a dipping method and spin coating, and subsequently the PL spectra of the planar samples was measured. The spectra also show blue-shift in photoluminescence caused by photo-oxidation as well.

Finally, two samples were fabricated by deposition of gold spheres and CdTe QDs on Si(100) substrates. The first sample was designed to demonstrate a quenching effect of PL. To confirm the quenching of PL on the manufactured sample, it is neccesary to have a reference sample, which requires more advanced measurement techniques. The second sample was designed to observe the PL enhancement caused by local field enhancement

at the excitation wavelength, but unexpected attraction was observed between the QDs and gold spheres by the SEM measurements. The possible solution to this problem would be the application of QDs with a capping layer on their surface to secure a neccesary distance in order to avoid PL quenching at short distances.

List of references

[1] PURCELL E. M.: *Spontaneous emission probabilities at radio frequencies*, Physical Rewiev 60, 674, 1946.

[2] KITTEL CH.: *Introduction to Solid State Physics, 8th edition*, John Wiley & Sons, New York, 2005.

[3] BOHREN C. F., HUFFMAN D. R.: *Absorption and Scattering of Light by Small Particles*, John Wiley & Sons, New York, 1983.

[4] DRUDE P.: *Zur elektronentheorie der metalle*, Annalen der Physik 306, 566-613, 1900.

[5] MAIER S. A.: *Plasmonics: Fundamentals and Applications*. Springer, UK, 2007, ISBN-10: 0387331506.

[6] SCHMIDT E., HUMLÍČEK J., LUKEŠ F., MUSILOVÁ J.: *Optické vlastnosti pevných látek*, Státní pedagogické nakladatelství, Praha, 1986.

[7] JACKSON J. D.: *Classical Electrodynamics*, John Wiley & Sons, New York, 1999.

[8] FARAHANI J. N.: *Single Emitters Coupled to Bow-Tie Nano-Antennas*, PhD Thesis, University of Basel, Basel, 2006.

[9] DUB P., PETRÁČEK J.: *Vybrané problémy z teorie elektromagnetického pole.* VUT, FSI, Brno, 2009.

[10] PELANT I., VALENTA J.: *Luminiscenční spektroskopie I*, Academia, Praha, 2006.

[11] FOX M.: *Optical Properties of Solids*. Oxford University Press, Oxford, 2001,

[12] GERSTEN J., NITZAN A.: *Electromagnetic theory of enhanced Raman scattering by molecules adsorbed on rough surfaces*, Journal of Chemical Physics 73, 3023-3037, 1980.

[13] CHANCE R.R., PROCK A., SILBEY R.: *Lifetime of an emitting molecule near a partially reflecting surface*, Journal of Chemical Physics 60, 2744-2748, 1974.

[14] Ruppin R.: Decay of an excited molecule near a small metal sphere, Journal of Chemical Physics 76, 1681-1684, 1982.

[15] ANGER P., BHARADWAJ P., NOVOTNY L.: *Enhancement and Quenching of Single-Molecule Fluorescence*, Physical Review Letters 96, 113002, 2006.

[16] SANDOGHDAR V. et al.: *Enhancement of Single-Molecule Fluorescence Using a Gold Nanoparticle as an Optical Nanoantenna*, Physical Review Letters 97, 017402, 2006.

[17] KUHN H.: *Classical Aspects of Energy Transfer in Molecular Systems*, Journal of Chemical Physics 53, 101-108, 1970.

[18] GEORGE T.F., KIM Y.S., LEUNG P.T.: *Classical decay rates for molecules in the presence of a spherical surface: A complete treatment*, Surface Science 195, 1-14, 1988.

[19] MERTENS H., KOENDERINK A. F., POLMAN A.: *Plasmon-enhanced luminescence near noble-metal nanospheres: Comparison of exact theory and an improved Gersten and Nitzan model*, Physical Review B 76, 115123, 2007.

[20] LAKOWICZ J. R.: *Radiative decay engineering 5: metal-enhanced fluorescence and plasmon emission*, Analytical Biochemistry 337, 171–194, 2005.

[21] Giannini V. et al.: *Controlling Light Localization and Light-Matter Interactions with Nanoplasmonics*, SMALL 6, 2498-2507, 2010.

[22] URL: <http://erbium.amolf.nl/index.php> (cit. 20.04.2012).

[23] NEUGEBAUER J. VAN de WALLE CH.G.: *Gallium vacancies and the yellow luminescence in GaN*, Applied Physics Letters 69, 503-505, 1996.

[24] KARLICEK R.F. et al.: *Microcavity effects in GaN epitaxial films and in Ag/GaN/sapphire structures*, Applied Physics Letters 70, 2790-2792, 1997.

[25] ŽÍDEK K. et al.: *Ultrafast photoluminescence dynamics of blue-emitting silicon nanostructures*, Physica Status Solidi C 8, 979- 984, 2011.

[26] PELANT I.: *Optical gain in silicon nanocrystals: Current status and perspectives*, Physica Status Solidi A 208, 625-630, 2011.

[27] WUISTER S. F., DRIEL A. F., van MEIJERINK A.: *Luminescence and growth of CdTe quantum dots and clusters***,** Physical Chemistry Chemical Physics 5, 1253-1258, 2003.

[28] BANG J.H., SUH W.H., SUSLICK K.S.: Quantum *Dots from Chemical Aerosol Flow Synthesis: Preparation, Characterization, and Cellular Imaging*, Chemistry of Materials 20, 4033-4038, 2008.

[29] LIGMAJER F.: *Depozice kovových nanocástic z roztoku a výzkum jejich optických vlastností*, Bakalářská práce, VUT, Brno, 2011.